Europe and the Future for WPT

COST Action IC1301 Team

This article presents recent European-based contributions for wireless power transmission (WPT), related to applications ranging from future Internet of Things (IoT) and fifth-generation (5G) systems to high-power electric vehicle charging. The contributors are all members of a European consortium on WPT, COST Action IC1301 (Table 1). WPT is the driving technology that will enable the next stage in the current consumer electronics revolution, including batteryless sensors, passive RF identification (RFID), passive wireless sensors, the IoT, and machine-to-machine solutions.

These new devices can be powered by harvesting energy from the surroundings, including electromagnetic energy, or by designing specially tailored beamed wireless energy to power them. In this respect, we can further separate the WPT beam in the near field and the far field, where *near field* implies normally inductive or capacitive coupling and *far field* implies RF transmission. In Europe, a group of universities, research institutes, and companies have joined efforts to achieve advances in this area. This consortium, Wireless Power Transmission for Sustainable Electronics (or "WiPE") and also known as COST Action IC1301, is a European Union framework for breakthrough science and technology.

Here, we summarize the most recent developments in research by some of the members of this group. The article is divided into three major technology discussions: far-field (WPT) developments, near-field developments, and WPT applications. Within the far-field approaches, we discuss such issues as waveform analysis and modeling of RF–dc converters, propagation modeling, and antennas specifically tailored for WPT schemes. For near-field approaches, we consider topics such as the optimized design of WPT inductive links and the modeling of these schemes, use of

---

The COST IC1301 WiPE Team is a group of researchers in Europe focusing on the study of efficient wireless power transmission circuits, systems, and strategies specially tailored for batteryless systems.
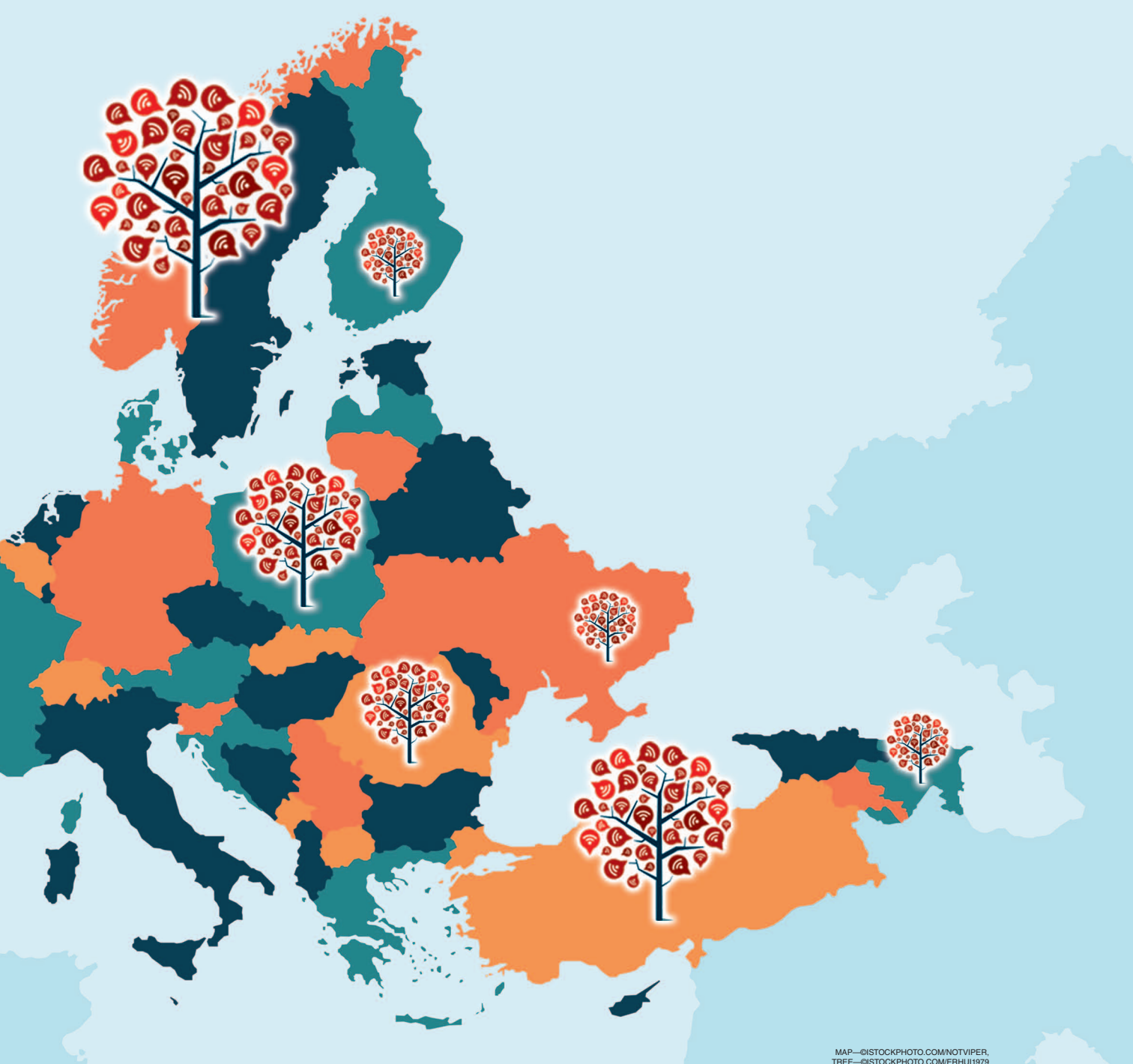
electrical resonance for transferring power across non-negligible distances, and underwater WPT. Finally, we discuss several applications, including integration of WPT in buildings, the use of such systems in wireless sensor networks (WSNs), embedding WPT schemes in car textiles, and using RFID schemes for improved efficiency.

Far-Field Deployments

Waveform Design for Maximizing RF–dc Conversion Efficiency

The power transfer efficiency of WPT systems is one of the most important parameters for the practical application of the technology. The total efficiency of a WPT system can be defined as

$$\eta_T = \eta_T \eta_L \eta_R, \tag{1}$$

where η_T is the transmitter's dc–RF conversion efficiency, η_L is the wireless link efficiency, and η_R is the receiver's RF–dc conversion efficiency. The various contributions to overall efficiency can be looked at in more detail by considering the individual efficiencies corresponding to specific system blocks, such as separating receiver efficiency into receive antenna efficiency, rectifier efficiency, and dc–dc converter circuitry efficiency contributions [1].

TABLE 1. COST Action IC1301 contributors to this article.

Name	Institution	Name	Institution
Nuno Borges Carvalho	Instituto de Telecomunicacoes, Universidade de Aveiro, Portugal	Mauro Mongiardo	University of Perugia, Italy
Apostolos Georgiadis	Heriot-Watt University, Edinburgh, Scotland, United Kingdom	Grigory Popov	University of Mons, Belgium
		Ning Pan	KU Leuven University, Belgium
Alessandra Costanzo	University of Bologna, Italy	Herve Aubert	CNRS–LAAS, University of Toulouse, France
Nobby Stevens	DraMCo Research Group, KU Leuven, Belgium	Federico Viani	ELEDIA Research Center, University of Trento, Italy
Jan Kracek	Czech Technical University in Prague, Czech Republic	Stavroula Siachalou	Aristotle University of Thessaloniki, Greece
Luís Pessoa	INESC TEC, Porto, Portugal	Przemyslaw Kant	SpaceForest Ltd., Poland
Luca Roselli	University of Perugia, Italy	Gianfranco Andia Vera	University Grenoble Alpes, Grenoble-INP, LCIS, Valence, France
Fortunato Dualibe	University of Mons, Belgium		
Dominique Schreurs	KU Leuven University, Belgium		
Senol Mutlu	Bogazici University, Istanbul, Turkey	Anastasis C. Polycarpou	University of Nicosia, Cyprus
Hendrik Rogier	University of Ghent, Belgium	Pedro Cruz	Universidade de Aveiro, Portugal
Huib Visser	IMEC, Eindhoven, The Netherlands	Franco Mastri	University of Bologna, Italy
Alexandru Takacs	CNRS–LAAS, University of Toulouse, France	Milos Mazanek	Czech Technical University in Prague, Czech Republic
Paolo Rocca	ELEDIA Research Center, University of Trento, Italy	Hugo Santos	INESC TEC, Porto, Portugal
		Federico Alimenti	University of Perugia, Italy
Antonis Dimitriou	Aristotle University of Thessaloniki, Greece	Hugo García-Vázquez	University of Mons, Belgium
		Sofie Pollin	KU Leuven University, Belgium
Jerzy Michalski	SpaceForest Ltd., Poland	Lorenzo Poli	ELEDIA Research Center, University of Trento, Italy
Zbynek Raida	Brno University of Technology, Czech Republic		
Smail Tedjini	University Grenoble Alpes, Grenoble-INP, LCIS, Valence, France	Daniel Belo	Universidade de Aveiro, Portugal
		Diego Masotti	University of Bologna, Italy
Wout Joseph	Ghent University/iMinds, Belgium	Jan Machac	Czech Technical University in Prague, Czech Republic
Yvan Duroc	University of Lyon, France	Vítor Tavares	INESC TEC, Porto, Portugal
John N. Sahalos	University of Nicosia, Cyprus	Paolo Mezzanotte	University of Perugia, Italy
Aggelos Bletsas	Technical University of Crete, Greece	Papy Ndungidi	University of Mons, Belgium
Theodoros Samaras	Aristotle University of Thessaloniki, Greece	Giacomo Oliveri	ELEDIA Research Center, University of Trento, Italy
Sotiris Nikoletseas	University of Patras, Greece, and Computer Technology Institute and Press "Diophantus," Greece	Ricardo Fernandes	Universidade de Aveiro, Portugal
		Henrique Salgado	INESC TEC, Porto, Portugal
		Véronique Moeyaert	University of Mons, Belgium
Theofanis P. Raptis	National Research Council, Institute of Informatics and Telematics, Pisa, Italy	Andrea Massa	ELEDIA Research Center, University of Trento, Italy
Alírio Boaventura	Universidade de Aveiro, Portugal	Ricardo Gonçalves	Universidade de Aveiro, Portugal
Ana Collado	Heriot-Watt University, Edinburgh, Scotland, United Kingdom	Pedro Pinho	Instituto de Telecomunicações, ISEL, Lisboa, Portugal
Riccardo Trevisan	University of Bologna, Italy	Giuseppina Monti	University of Salento, Italy
Ben Minnaert	DraMCo Research Group, KU Leuven, Belgium	Luciano Tarricone	University of Salento, Italy
		Marco Dionigi	University of Salento, Italy
Milan Svanda	Czech Technical University in Prague, Czech Republic	Peter Russer	Technical University of Munchen, Germany
Mário Pereira	INESC TEC, Porto, Portugal	Johannes Russer	Technical University of Munchen, Germany

In an attempt to maximize the obtained efficiency, recent literature has investigated the effect of the transmitted signal waveforms on the RF–dc conversion efficiency of rectifier circuits [2], [3] (Figure 1). Initial results have shown that signals with peak-to-average power ratio (PAPR) greater than 3 dB, which corresponds to the PAPR of a pure sine wave, may lead to a higher RF–dc conversion efficiency compared to continuous wave (CW) signals. The effect of different signals with a time-varying envelope, such as chaotic waveforms [4] and various digitally modulated signals and white noise [5]–[8], on RF–dc conversion efficiency has been investigated. The results show that it is possible to obtain better RF–dc conversion efficiency compared to CW signals using signals with a high PAPR. This can occur under certain average input-signal power levels as well as under certain output-load conditions [9].

Additionally, the complementary cumulative distribution function of a signal reveals detailed information about the number and frequency of signal peak occurrences relative to its average value, and signals with the same PAPR can lead to a different RF–dc conversion efficiency [9]. Depending on the application requirements that define a target input average power and output load, one may synthesize a signal waveform that maximizes the RF–dc conversion efficiency, such as the so-called multisine signals [10]. These signals are composed of a sum of sine waves equally spaced in frequency by Δf and, usually, $\Delta f \ll f_c$. It can be shown that, if all the subcarriers are added in phase, the resultant time-domain signal exhibits a high PAPR value that depends on the number of subcarriers and their spectral weight distribution.

Another important consideration is that the envelope is a periodic signal, with its period being inversely proportional to the frequency spacing (Δf). A small value for this Δf is desired to increase the number of subcarriers in a limited bandwidth; however, a small Δf leads to a very long envelope period, decreasing the frequency at which the output filtering capacitor is refreshed. Thus, multisine signals should be carefully designed and must take into account receiver characteristics such as the low-pass filter time constant.

To increase the output filtering capacitor's refresh rate, the work reported in [13]–[15] proposes a new type of multisine signal. Using subcarriers that are harmonically related ($\Delta f = f_0$), the envelope's peak frequency will be as high as the first subcarrier frequency, reducing the constraints on the output low-pass filter's time constant. Moreover, if the subcarriers are equally weighted and in phase, the time-domain waveform is asymmetric, with high positive peaks and low negative peaks. This asymmetric characteristic will boost the efficiency not only in low-power environments due

These new devices can be powered by harvesting energy from the surroundings, including electromagnetic energy, or by designing specially tailored beamed wireless energy to power them.

to its high PAPR (such as conventional multisines) but also in high power, when the diode is operating near its breakdown (asymmetry reduces the peak-to-peak swing). Because of the harmonic relation between carriers, several intermodulation products generated by the rectifying process will contribute to a dc increase.

Another type of high PAPR waveform suitable for WPT is proposed in [14]. Following radar fundamentals, a linear frequency-modulated signal known as a *chirp signal* is considered. If an up-chirp is correlated with a down-chirp (a pulse-compression technique), a pulse will be created, and its high PAPR and occurrence can be controlled with the basic chirp bandwidth and frequency sweep time. The occurrence of the pulse should be carefully controlled to avoid a large ripple in the output, which in turn reduces the output dc voltage. Due to its very high PAPR, this kind of signal will drive the rectifying element into its breakdown zone for lower input power when compared with other excitations.

Finally, we should emphasize that the absolute value of the RF–dc conversion efficiency strongly depends on the nonlinear device and circuit architecture characteristics of the rectifier, and it is possible to improve the obtained efficiency by combining
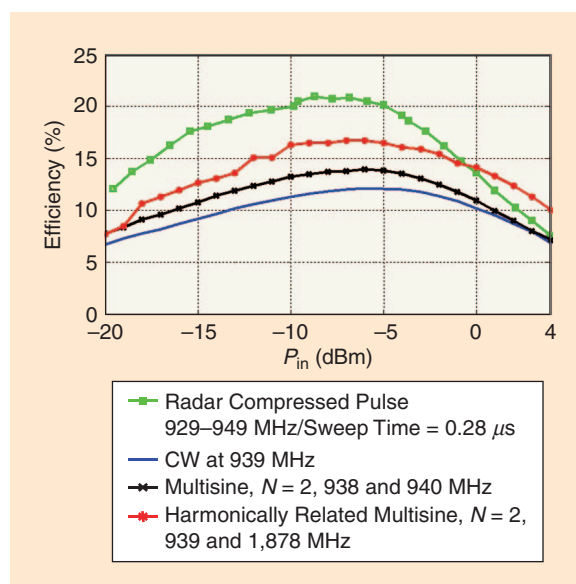

Figure 1. *A comparison of RF–dc conversion efficiency with different waveforms.*

The power transfer efficiency of WPT systems is one of the most important parameters for the practical application of the technology.

WPT with other energy harvesting technologies such as mechanical [11] or thermal [12].

Modeling Aspects of RF–dc Conversion

After realizing the advantage of multisine excitation for WPT, it becomes necessary to understand the impact of various design parameters such as bandwidth or the number of tones. In [16], the multisine signal is represented as an amplitude-modulated signal (2) with bandwidth B (3):

$$x(t) = A_m \cos(2\pi f_c t), \qquad (2)$$
$$B = N_t \cdot \Delta f. \qquad (3)$$

Here, f_c is the carrier frequency, A_m is the envelope of the signal, N_t represents the number of tones, and Δf their frequency spacing.

Given this signal representation, the analytical RF power-conversion efficiency (PCE) ($PCE = (V_{DC}/R_L \cdot p_{in})$) is calculated by relating the bandwidth and envelope amplitudes to the output dc voltage V_{DC} for different signals by applying

$$V_{DC} = \int_0^{N_{period}} V_{out}(A_m) \cdot Pdf(A_m).dt. \qquad (4)$$

$Pdf(A_m)$ is the probability distribution function of the envelope amplitude as triggered by the multisines. V_{DC}, as described in (4), is the average function of instantaneous output voltage V_{out} depending on different A_m, reflecting the input-power-dependent performance of rectifiers.
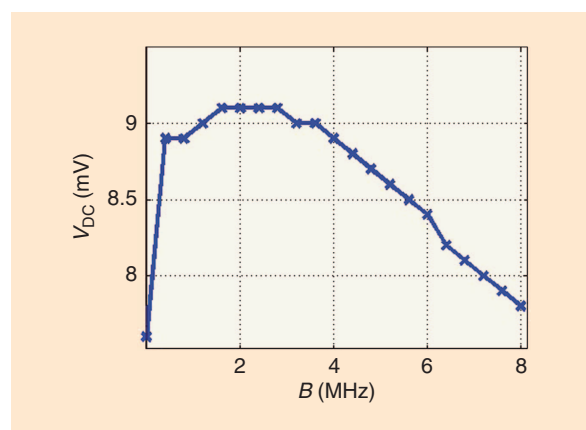
The input signal to the rectifier $x_i(t)$ is the multisine signal $x(t)$, where parts of the signal are reflected due to circuit mismatches that depend on the B of the input signal $x(t)$. As a result, B and circuit mismatches also change $Pdf(A_m)$. By studying the reflection coefficient S_{11} of the given rectifier, we can select the optimal bandwidth of the signal. For the circuit used in this analysis, the optimal B is 2 MHz, as shown in Figure 2. Knowing that the number of tones N_t influences both the B and amplitude shape $Pdf(A_{m,i})$ of $x_{in}(t)$, the optimal N_t can be determined using the mathematical model described earlier.

The analytical results are confirmed by measurements. The measurement configuration is shown in Figure 3. Depending on the rectifier used in this experiment, the PCE of the multisine-based WPT system can be improved 25.1% compared to a CW excitation WPT for −5-dBm input power, as shown in Figure 4.

Link Modeling and Integrated Antenna Design Strategies for Ultrawide-Band WPT

The IoT vision requires the deployment of vast amounts of wireless nodes that are invisibly integrated into their environment. Important challenges when designing such nodes include ensuring sufficient autonomy to guarantee reliable wireless communication over sustained periods of time, while avoiding interference with other devices. For compactness and eco-friendliness, the use of large batteries should be avoided, and small energy buffers such as super-capacitors should be preferred. Therefore, the device should be able to continuously harvest energy from multiple sources available in its environment. Intentional WPT may supplement the powering process, or it may act as the only power supply in cases where all energy sources are scarce.

Interference issues and health risks associated with the transmission of RF power beams may be avoided by lowering the power spectral density. This is achieved by spreading out the radiated power over a large frequency band. Such a technique is already applied
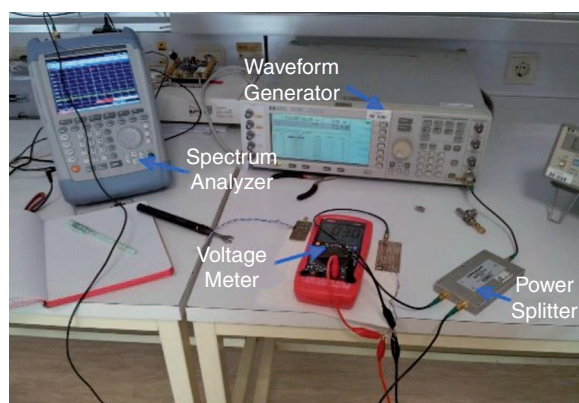
Figure 2. V_{DC} versus B, with RF signal input power of −5 dBm and 1.6 GHz carrier frequency.

Figure 3. The measurement configuration for the tests described in the "Modeling Aspects of RF–dc Conversion" section.

in ultrawide-band (UWB) communication, which is allowed by the U.S. Federal Communications Commission in the 3.1–10.3-GHz frequency band, provided that the power spectral density remains smaller than −41.3 dBm/MHz [17]. Similarly, the European Commission (EC) has issued an EC decision allowing UWB devices to use the 3.4–4.8- and 6.0–8.5-GHz bands with the same maximum power spectral density, provided that signals in the lower frequency band meet a low duty-cycle restriction [18].

An important challenge for implementing such UWB WPT in an IoT setting is that wireless nodes will operate in a diverse range of deployment scenarios. In most of them, many objects will be present in close proximity to the receive antenna, causing potential antenna detuning and reduction in radiation efficiency. Moreover, the WPT wireless channel will differ significantly from free space, as important shadowing and multipath fading effects may occur. Therefore, we have developed robust high-performance UWB antennas and a dedicated block model that describes all antenna and multipath propagation characteristics that play a role in the complete wireless power link. Both components enable the development and optimization of stable UWB WPT links, operating in all kinds of adverse deployment conditions. They enable optimal exploitation of the large bandwidth through the design of suitable waveforms, and they maximize WPT while still respecting safety and health regulations.

Designing UWB antennas for the IoT paradigm is highly complex. Deployment conditions require antennas featuring a high antenna/environment isolation for stable radiation. A low-profile, compact, and adaptable geometry that also conforms to the environment is needed for invisible integration. Such antenna topologies typically exhibit narrow-band radiation characteristics. Recently, the implementation of substrate integrated waveguide (SIW) technology in novel antenna materials such as textile fabrics [19], paper, and cork [20] has resulted in novel designs that reconcile all these requirements. By confining the electromagnetic fields by rows of vias, components operate in isolation from their environment, yielding a performance almost as stable as in waveguide components [21]. For cavity-backed SIW slot antennas, such as the antenna array shown in Figure 5, only the slot radiates, thus enabling the deployment of active circuitry directly underneath and energy harvesters on top of the cavity [22]. The complete antenna area may be reused, apart from the radiating slot. UWB operation is implemented by exciting multiple cavity modes at carefully selected frequencies within the operational bandwidth. Moreover, the antenna may be miniaturized by exploiting half-mode and quarter-mode principles.

Besides using a suitably designed antenna, the optimization of the WPT channel requires that the wireless channel characteristics and the deployment

Multisine signals should be carefully designed and must take into account receiver characteristics such as the low-pass filter time constant.

characteristics of the antennas be fully taken into account. Indeed, multipath propagation will affect the power transfer, causing fading and shadowing effects as experienced in conventional communication channels. Furthermore, because they are in the reactive near field, objects in direct proximity to the transmit and/or receive antennas will modify the channel's power transfer characteristics. Therefore, they should also be included in a global WPT model applied to optimize the power transfer.

As a computer-aided-engineering tool for UWB WPT system designers, we have developed a modeling framework [23] for WPT over UWB links in multipath propagation environments. Although the concatenated black-box model is specifically implemented for WPT
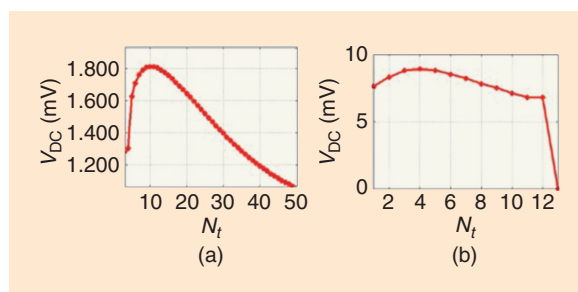

Figure 4. V_{DC} behavior with increasing Nt; the RF signal input power is −5 dBm, and carrier frequency is 1.6 GHz. (a) The Matlab simulation result and (b) the measurement result.
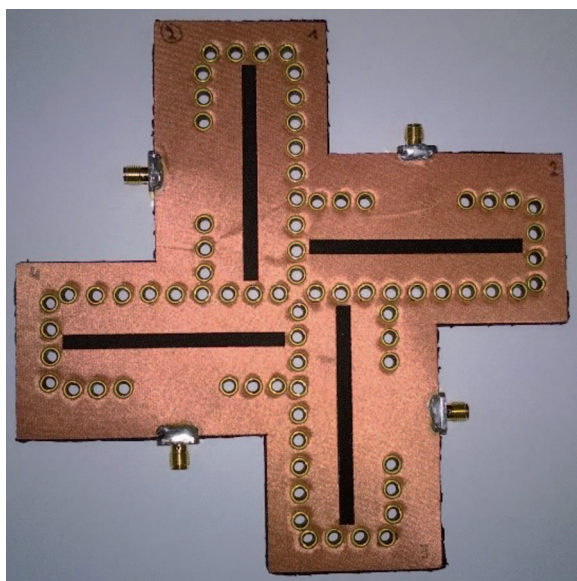

Figure 5. A UWB SIW textile antenna array for WPT.

The IoT vision requires the deployment of vast amounts of wireless nodes that are invisibly integrated into their environment.

in the vicinity of the human body, the framework may also be successfully applied to other typical IoT configurations. The modularity of the model makes it easy to replace the measured or simulated black-box descriptions of the antennas and the channel by those that are pertinent to the setup at hand. Proximity effects caused by objects in the reactive near field of the antenna may easily be accounted for by incorporating the embedded active-element antenna pattern and the detuned antenna impedance in the black-box description of the antenna under study. For the application of this model to body-centric WPT, we refer to [24]. By relying on a fast-multipole-based expansion of the channel [24], the Friis-based path-loss black box may be extended such that the channel model also applies to the radiative near field.

Efficient Miniature Rectennas with Integrated Power Management for Battery Replacement

Using a small rectenna and thus a small receiving antenna will result in a small dc output voltage. Therefore, an integrated circuit (IC) is needed for boosting this voltage up to the desired voltage. The

circuit needs to be powered by the low-voltage, low-power dc signal available. For our prototype, we chose the Texas Instruments TI BQ25570 ultralow-power harvester power-management IC [25]. The converter can cold-start from 0.33 V dc and after this cold start can continue on 0.10 V dc. The output dc voltage can be chosen to be between 1.3 and 4.0 V, using the internal buck converter.

The circuit has been tested by connecting a voltage-doubling rectifier [26] to a signal generator, using a lumped-element LC impedance-matching network in between the two. The output of the power-management IC is dynamically loaded using an array of load resistors. These load resistors are connected to switch-operating field-effect transistors. The switches are (time) controlled using an Arduino megaboard [27] with an AT mega2560 Atmel microcontroller. The test system is shown in Figure 6.

In Figure 6, η_r is the RF–dc PCE of the rectifier circuit with the matching network, η_h is the overall efficiency, and η_{b1} is the RF–dc PCE of the rectifier with the matching circuit combined with the boost converter, as described in [28]. The boost converter PCE η_b and buck converter PCE η_{b2} can be found from the earlier defined PCEs [28].

For a constant on-time t_{on} and a constant load resistance, the maximum values of η_r, η_h, η_{b1}, η_b, and η_{b2} are obtained at 868 MHz for different RF input power levels by varying the off-time t_{off} (see Figure 6). The results are shown in Figure 7.

Using the Friis equation, an assumed 3-W effective isotropic radiated power (EIRP) at 868 MHz, and
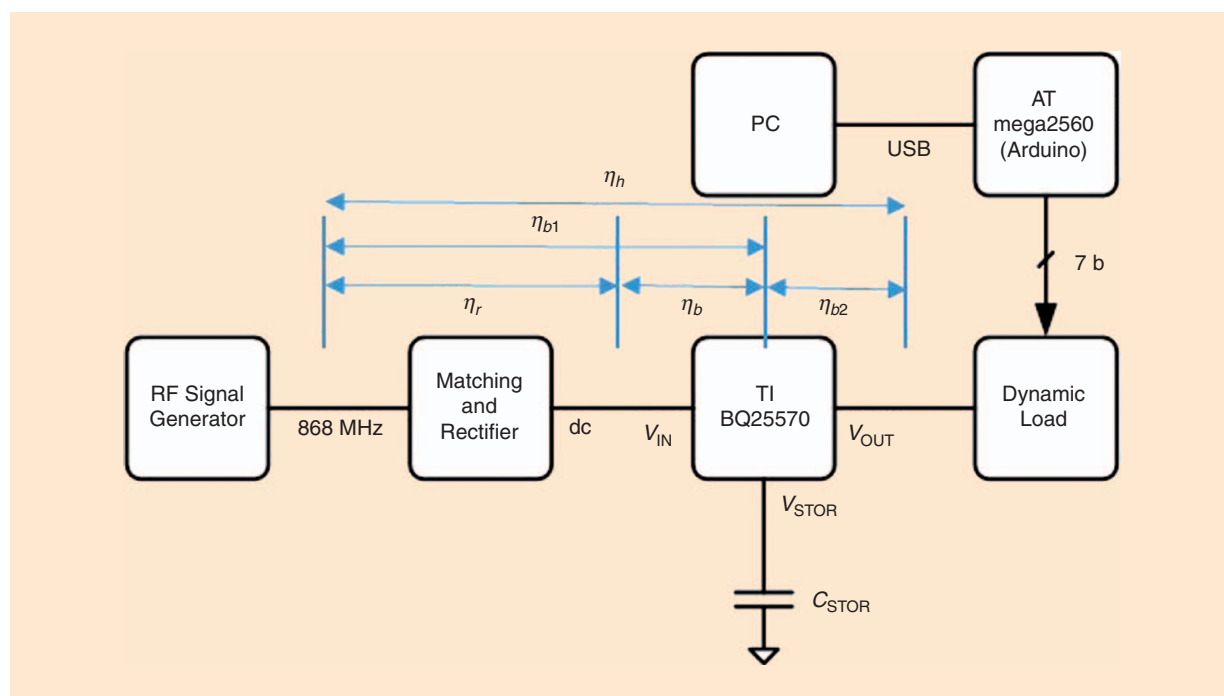

Figure 6. *A rectenna test circuit. The antenna is replaced by a signal generator. Energy is stored in capacitor C$_{STOR}$. The circuit is designed for and tested at 868 MHz. PC: personal computer.*

the results shown in Figure 8, the average obtained dc power has been calculated as a function of distance for two receive antennas (1- and 6.1-dBi gain). The results are shown in Figure 9.

From Figure 7 and Figure 9, we can conclude that with a 6.1-dBi receive antenna we can get 30 μW of continuous dc power up to a 10-m distance or 60 mW for 40 ms every 2 min up to the same distance.

For a prototype, a 2-dBi miniaturized 915-MHz antenna [29], complex-conjugately matched to the rectifier, has been combined with the TI BQ22570 IC, resulting in a 10-cm × 6-cm wireless battery, as shown in Figure 10.

Compact Microwave Rectenna for Satellite Health Monitoring

To provide reliable high-bit-rate broadcasting links, high-gain microwave antennas are used on broadcasting satellites. Thes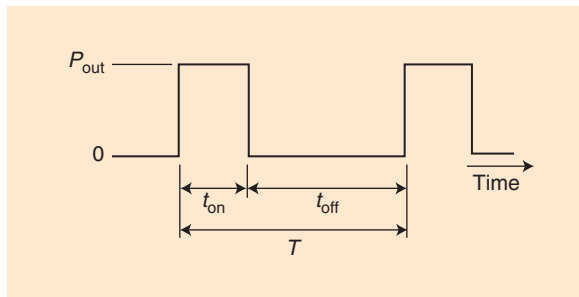e antennas are located on panels positioned on the external surfaces of the satellite and are subject to spillover losses. In some areas of the antenna panels, the electric field generated by the spillover losses of microwave antennas may reach the following maximum levels (effective values) [30]: 40 V/m in C-band, 49.5 V/m in X-band, 106 V/m in Ku-band, and 127 V/m in K-band. These electric field levels are unusual for terrestrial applications, but they can occur on satellites when data links are functional. These (residual) electromagnetic fields can be harvested to power-autonomous wireless sensors for structural health monitoring of the satellite. The radiated power of microwave antennas is almost constant; consequently, the dc power regulatory circuits should be minimal for such harvesting systems.

To demonstrate the proof of concept and feasibility of such harvesters, several rectennas were developed by the research group at CNRS-LAAS Toulouse [31] in the framework of research grants funded by CNES (the French space agency). The goal was to

Figure 7. *A time diagram of drawing dc power from the circuit shown in Figure 6. T is the period. During t_{on}, a dc power P_{out} is drawn. During t_{off}, no power is drawn.*
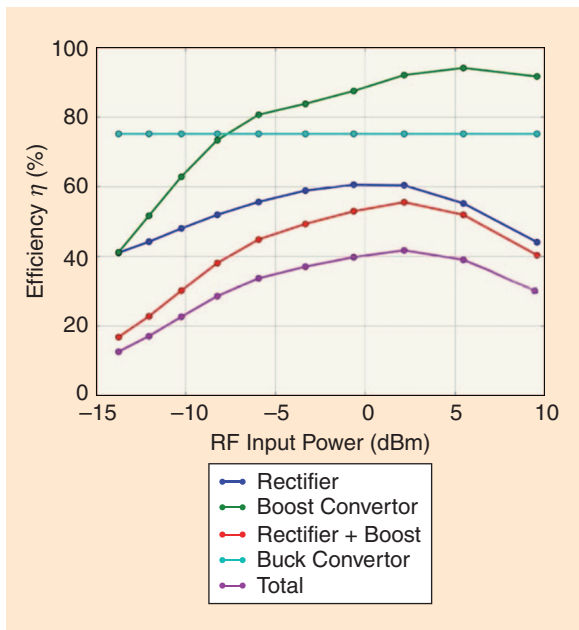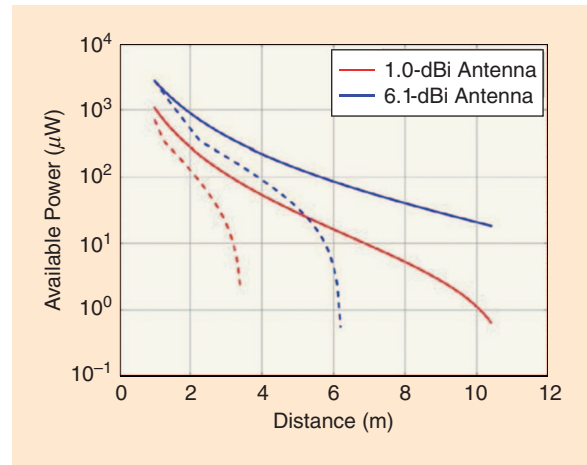

Figure 9. *The average obtained dc power versus free line-of-sight distance for two antennas. The solid lines represent the results for the circuit described in Figure 6. The dashed lines represent the results for a commercially available radiative WPT system tested for the same EIRP but for a frequency of 915 MHz.*
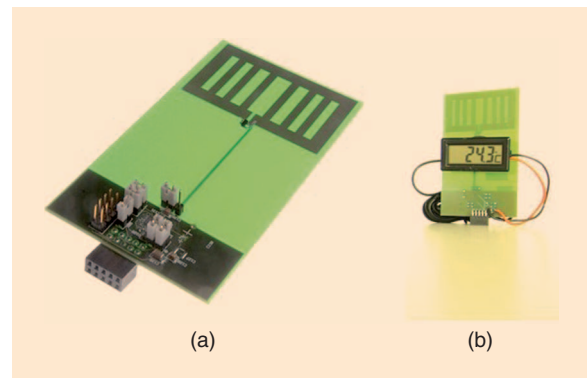

Figure 8. *Maximum PCEs as a function of RF input power level for the setup shown in Figure 6.*

Figure 10. *A printed circuit board (PCB)-integrated rectenna and its power management: (a) the PCB and (b) the system powering a temperature sensor with display.*

develop compact, high-efficiency rectennas providing dc power in the milliwatt range. Based on innovative antenna topologies, the cross-dipole antenna (CDA) and CDA array (CDAA), we recently proposed compact coplanar stripline-supported rectennas. Figure 11 shows the CDA rectenna topology, while the CDAA rectenna is depicted in Figure 12.

CDA rectennas use only the top side of the PCB. In the case of a CDAA, the antenna and the diode are located on the top side of the PCB, while the shorting RF capacitor and the load are located on the bottom side. The conjugate matching condition (between antenna and rectifier) is achieved without the use of a dedicated matching circuit but by properly controlling the input impedance of the antenna (CDA or CDAA) and the input impedance of the rectifier. 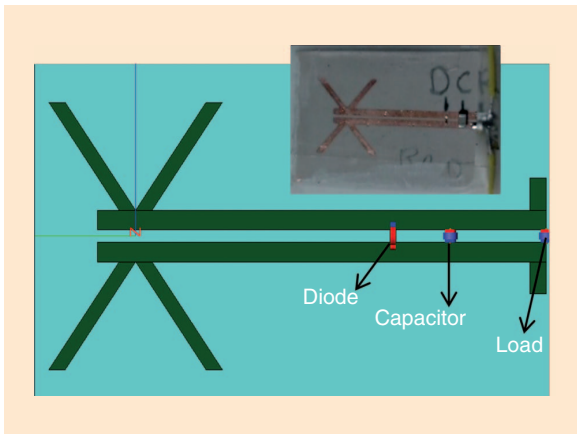A reflector plane, positioned below the rectennas at an approximately quarter-wavelength distance, is used to increase the antenna gain and thus improve the overall performance of the CDA and CDAA rectennas.

The efficiency η (in %) of the rectenna can be computed using the following [32]:

$$\eta_1 = \frac{P_{DC}}{S \cdot A_G} \cdot 100 \tag{5}$$

$$\eta_2 = \frac{P_{DC}}{S \cdot A_{\text{eff}}} \cdot 100 = \frac{4 \cdot \pi \cdot P_{DC}}{S \cdot G_R \cdot \lambda^2} \cdot 100, \tag{6}$$

where P_{DC} is the harvested dc power, S is the incident electromagnetic power density, A_G denotes the area of the radiating surface, A_{eff} is the antenna effective area, G_R is the gain of the antenna, and λ is the wavelength of the illuminating electromagnetic wave. The efficiency η_1 can be viewed as a "worst-case" definition, because $A_{\text{eff}} \leq A_G$ for passive antennas.

Experimental results [33] show that 1.15 mW of dc power can be harvested in the Ku-band (14.7 GHz) using a compact CDAA rectenna illuminated by an electric field of 60 V/m ($S \sim 955\ \mu\text{W/cm}^2$). This ultracompact Ku-band CDAA rectenna (2.5 cm^2 or 0.6 square wavelength) exhibits a conversion efficiency of $\eta_1 = 48\%$ ($\eta_2 = 66\%$). A low-cost silicon Schottky diode (SMS201 from Aeroflex/Metelics) in a molded plastic (dual flat no-lead) package was used for this design. A manufactured K-band (18.8 GHz) CDA rectenna (using a gallium arsenide Schottky diode MZBD-9161 from Aeroflex/Metelics) [30] demonstrated that a dc power of 1.28 mW can be harvested when an electric field of 91 V/m ($S \sim 2.2\ \text{mW/cm}^2$) illuminates the rectenna. The efficiency of this CDA rectenna is $\eta_1 = 48\%$. We note that CDA and CDAA rectenna topologies can be easily adapted for other operating frequencies. The experimental results obtained with these rectennas demonstrate that implementing autonomous wireless sensors can be a feasible solution for the structural health monitoring of satellite antenna panels.

Figure 11. *The top view of the CDA rectenna and (inset) a photo of the manufactured prototype.*

Figure 12. *The top and bottom layers of the CDAA rectenna and (inset) a photo of the manufactured prototype.*

Design and Optimization of Phased Arrays for Long-Range WPT

The design of phased-array antennas is key to guaranteeing high-efficiency, reliable, and cost-effective long-range WPT system deployments [34]. Unlike communications and radar applications, the goal of a WPT system is to maximize end-to-end power transfer efficiency. Therefore, unconventional constraints need to be taken into account and, consequently, unconventional design methodologies explored [34a]. For long-range WPT systems, the transmitting array must focus power within a narrow, angular sector toward the receiving station or stations, while the receiving (i.e., rectenna) array must be able to convert the largest amount of RF impinging power. In this framework, several research projects have been carried out over the last few years, spurred by the diffusion of electrical

autonomous systems (e.g., drones, cars, and high-altitude platforms) and growing interest in the very challenging and fascinating application of space-based solar power (SBSP), which is aimed at guaranteeing a continuous feeding of the Earth with renewable and clean energy [35]. Novel methodologies for the design of arrays for long-range WPT and the optimization of their degrees of freedom (DoFs) have been introduced aimed at

- defining the best array configurations (e.g., positions and excitation weights of the array elements) to maximize 1) the beam collection efficiency (BCE), i.e., the ratio of the power transmitted toward the receiving/target area and the total radiated power, in the case of transmitting arrays or 2) the efficiency of the microwave power collection in the case of rectenna arrays
- synthesizing simplified array architectures to reduce antenna complexity and cost as well as to make the hardware/software implementation easier.

As for the optimal design of transmitting planar phased arrays, a strategy for synthesizing the optimal tapering of the amplitude weights that guarantees maximum BCE performance in cases of arbitrary transmitting planar apertures and target areas has been proposed in [36]. The approach, based on the solution of a generalized eigenvalue problem by means of a deterministic method, has allowed study of the theoretical limits of the power transmission efficiency of WPT planar phased arrays. Useful guidelines on the design of the transmitting array configuration have been reported to achieve high values of BCE (close to 100%), whatever the shape of the transmitter and/or receiving area. As a representative example, Figure 13(a) shows the power pattern generated by a planar array consisting of 20×20 elements, the excitation amplitudes of which [Figure 13(b)] have been synthesized by means of the method described in [36] to achieve a BCE performance of 99.96%.

Work regarding receiving antennas for long-range WPT has focused on studying and defining innovative rectenna arrays for SBSP systems to be used in the ground station. Starting from the key observation that the dc currents at the output of the rectifying circuitry used for each individual element or cluster of elements have no phase term (and, consequently, their coherent sum is not needed), the position of the elements has been properly optimized to avoid superpositions and shadowing effects that would reduce end-to-end WPT efficiency [37]. Moreover, because a portion of the microwave power arriving on the rectenna array is unavoidably backscattered, the DoFs of the element positions have been defined such that the reradiated field is focused toward a mirror that can redirect the power toward the rectenna array [37].

As a computer-aided-engineering tool for UWB WPT system designers, we have developed a modeling framework [23] for WPT over UWB links in multipath propagation environments.

Innovative array architectures to reduce the complexity and weight of the transmitting arrays have been studied, as well. Two strategies, in particular, have been investigated: 1) clustering the elements into subarrays to reduce the number of amplifiers and phase shifters/delay units and 2) using irregular (e.g., sparse) array layouts to minimize the number of radiating elements [38]. Optimization of the arrays' DoFs has been carried out by means of ad hoc design methodologies. As for clustered arrays, an excitation matching approach based on the contiguous partition method (CPM) [39] has been exploited to define the clustering configuration and the subarray excitations so as to obtain a pattern as close as possible to the one having optimal BCE [36]. The availability of the optimal excitations has enabled, through the CPM, the effective synthesis of very large phased arrays, not feasible when using conventional design methods.

The design of sparse planar arrays matching a desired reference pattern has been addressed by means of an innovative synthesis method based on Bayesian compressive sensing (BCS) [40]. The key advantage of the BCS methodology is that it allows light-transmitting arrays with a minimum number of elements. Preliminary results have shown that BCS-designed array configurations with a 35% reduction in the total number of elements guarantee a BCE-optimal power pattern by considering the same antenna aperture. Further studies in this area of research will consider the design of arrays with more complex geometries (e.g., conformal) as well as the use of simpler feeding networks characterized, for example, by isophoric (i.e., uniform) amplitude weights.

Far-Field Channel Modeling for WPT Systems

Well-designed, efficient WPT systems often fail in the application field due to undesired effects caused by the propagation channel. The power limitations of WPT systems, imposed by the turn-on voltage of the front-end diodes, require careful field installations and good prediction of the channel so that most of the available RF power will be harvested. Far-field WPT systems are found at frequencies starting from 100 MHz up to several gigahertz, with the most common application field, being passive UHF RFID technology around 900 MHz.
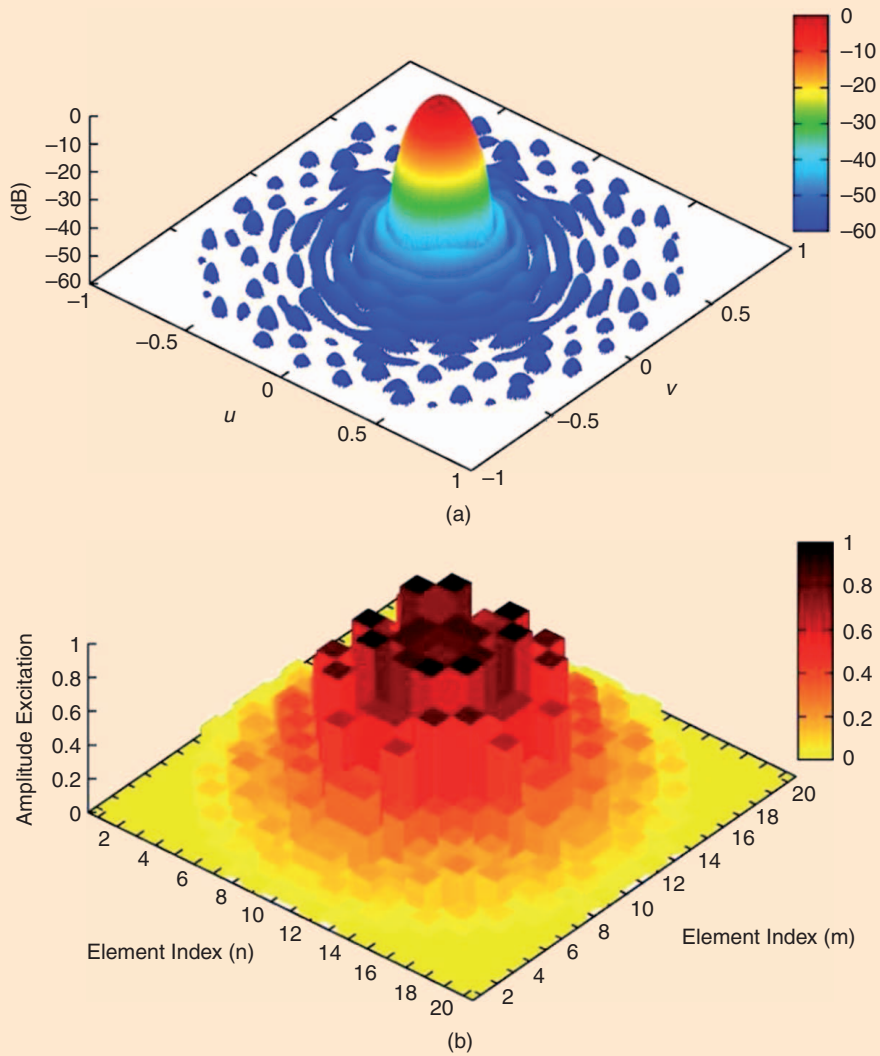
Figure 13. *The (a) power pattern and (b) distribution of the amplitude weighting coefficients of an optimal Slepian planar array.*

The necessary minimum input power (~ −20 dBm) for the operation of batteryless devices imposes specific limitations in the associated propagation channel. Unobstructed line-of-sight conditions between the transmitter and the passive device must exist. The transmitted electromagnetic signal reaches the receiver from other paths after interacting with the environment (scattering, reflections, diffractions, etc.) and interacts with the strong line-of-sight contribution constructively or destructively depending on the phase of each multipath component. This process creates fading, which varies in time depending on the variability of the propagation environment. Careful modeling of the environment and the transmit-receive system is necessary, including the radiation patterns and polarizations of the antennas, the geometrical and electromagnetic characteristics of the surrounding environment, and so forth. Simplified path-loss models, not accounting

for fading, should be avoided. Suitable candidates for WPT channel modeling are analytical ray-tracing models, computational electromagnetic models, and probabilistic models.

In [41], [42], an analytical ray-tracing model is developed to analyze the fading patterns in typical indoor WPT application areas. Methods to improve the performance of passive UHF RFID systems are proposed. For instance, it is shown that by deploying two transmit antennas illuminating the same region and connecting a 180° phase shifter in one of them, one can eliminate "holes" (destructive interference patterns) inside the area of interest by changing the phase of one of the antennas in a sequential manner, boosting the performance of the WPT systems. Furthermore, multiantenna configurations are analyzed that could be used when minima of the field are desired in specific locations, e.g., above the bed of a patient.
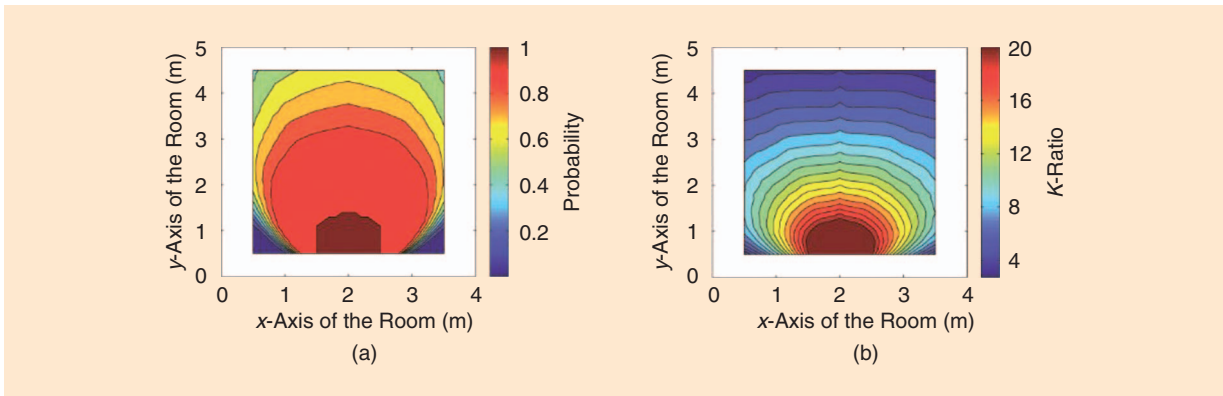
Figure 14. *The characteristic result of the probabilistic model in [44]. (a) The probability of reception* x *polarization and (b) the Rician distribution K ratio (dB) for* x-*polarized tags.*

Ray-tracing propagation modeling delivers accurate predictions, provided that the actual environment is exactly as modeled. However, this is not possible for the majority of applications, where walls and furniture are incorrectly modeled (geometrically or/and electromagnetically). Furthermore, such models output a static screen shot of the field with maxima and minima at fixed locations, implying that the field pattern will remain unchanged, and do not accommodate the reality of the fast-changing environment. Finally, even though they are much faster than computational electromagnetic models (CEMs), ray-tracing methods are still very slow to handle problems of automated planning (deployment) of WPT networks. Clearly, CEMs suffer from all the aforementioned disadvantages, plus they require vast amounts of memory and time. Nevertheless, CEMs provide the most accurate estimations for problems with known geometry in well-defined spaces, e.g., the field of a shelf antenna inside a library [43].

To overcome, these limitations a fast, site-specific probabilistic model was developed exploiting the particularities of WPTs, due to the power constraints of the system, while carefully considering all significant propagation factors that affect the accuracy of the estimations [44]. The probability that the power is above a specified threshold is derived for any antenna and any polarization axis. The model overcomes the limitation of delivering an unrealistic stationary output field. In fact, it cannot predict the location of a minimum or a maximum; however, it can evaluate the probability that such an event might happen.

The model exploits the existence of a strong power component in WPT systems and models the reception level by a Rician probability density function:

$$f(x \mid \nu, \sigma) = \frac{x}{\sigma^2} e^{\left(\frac{-(x^2 + \nu^2)}{2\sigma^2}\right)} I_0\left(\frac{x\nu}{\sigma^2}\right), \tag{7}$$

where ν^2 is the power of the line-of-sight strong component and $2\sigma^2$ is the mean power of the other contributions. Therefore, by calculating these two parameters

at each location inside the area of interest, one can estimate the probability that the reception magnitude x is greater than a given threshold y (see, e.g., Figure 14).

Further, in [44] all multiply-reflected rays initially bouncing on the same obstacles are clustered in a single "super-ray." Then, the contribution of this super-ray is approximated by a closed-form equation; the key to derive the equation is to treat the phases of each ray within the cluster as random variables, identically and uniformly distributed over $[0 - 2\pi]$. The success of the model is that the output probability carefully considers the radiation patterns, the polarization of the involved antennas, and the geometry and electromagnetic properties of the surrounding environment, similar to an analytical ray-tracing model. The key assumptions of the model are validated against ray tracing and measurements in [45]. The probabilistic model is compared to a finite-difference time-domain (FDTD) model in [46] along with additional measurements. A realistic model of the environment was inserted in the CEM model (Figure 15), including all furniture, and measurements were conducted in the same area. Both models demonstrated similar performance in terms of accuracy; in fact, the probabilistic model was slightly better (1.7% root-mean-square error versus 3.6% of the CEM model), as shown in Figure 16. The simulationtime was 135 h for the CEM model in an advanced workstation and less than a minute for the probabilistic model running on a laptop. Finally, the
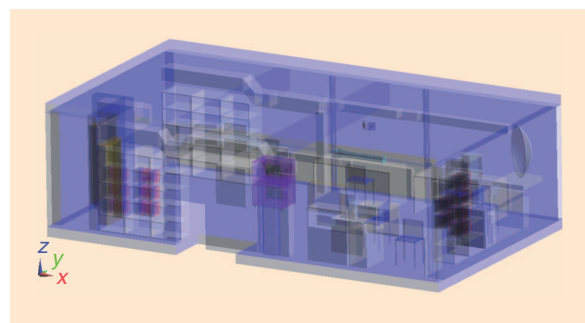

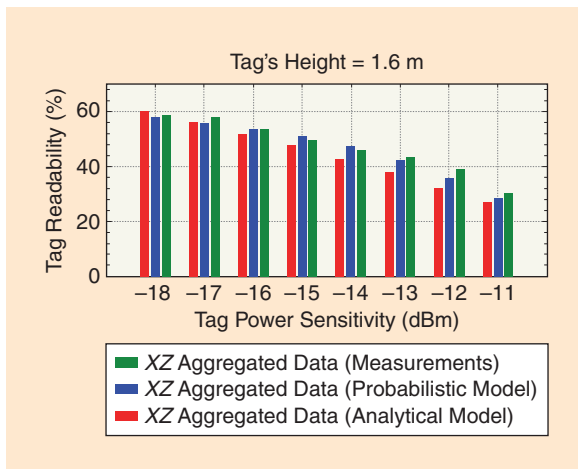**Figure 15.** *A detailed model of the measurements' area in [45].*

Figure 16. *A comparison of the model proposed in [45], the CEM, and measurements.*
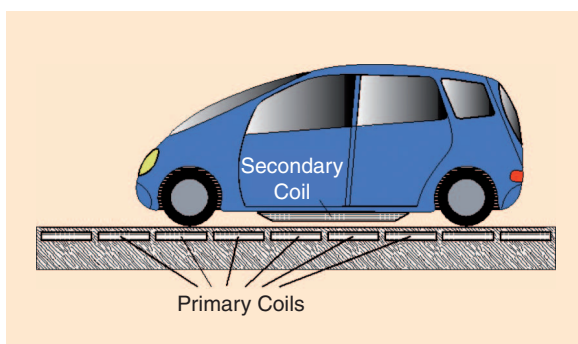

Figure 17. *The coil arrangement in the MFIPT system from [57].*

proposed model is exploited in a deployment problem in a large area and is combined with a particle swarm optimization method to deliver a deployment solution satisfying specific constraints [47].

Near-Field Deployments

Simultaneous WPT and Near-Field Communication

Theoretical and Numerical Contributions
To realize mid-range magnetic resonant WPT (MRWPT) systems, the efficiency of the system has been optimized by numerical electromagnetic modeling [48]–[50]. In [48], a MRWPT system consisting of electrically and magnetically coupled spiral resonators and loop inductances was presented. In [48] and [49], the experiment reported in [50] was reproduced using a full-wave simulation. An approach considering the WPT link as a two-port network has been used. A theoretical investigation was performed [49] to find, for a given WPT link, the load values that maximize either efficiency or the power on the load. In [51], a unified approach was proposed for energy harvesting and WPT. In [52], we presented the rigorous network modeling of several concepts for realizing efficient MRWPT. We

implemented the ideally required 1:*n* transformer using immittance inverters. We derived series and parallel matching topologies for maximum WPT [53].

Inductive Power Transfer for Electric Vehicles
The possibility of using inductive power transfer for electric vehicles has been considered in [54]–[57]. This moving-field inductive-power transfer (MFIPT) system for supplying power to electric vehicles while driving uses primary coils arranged below the pavement along the route for transmitting the energy via an alternating magnetic field to a secondary coil located on the vehicle below its floor (see Figure 17). To minimize losses, only the primary coils located below the secondary coil of a vehicle are excited. The operating principle of this MFIPT system is based on a resonantly operated switched dc–dc converter, converting the dc power supplied by the stationary power line to dc power delivered to the moving electric vehicle.

Contactless power supply of electric vehicles on highways allows low battery capacities because the batteries are required only in local traffic and on side roads where no MFIPT system would be installed.

Inductive Power Transfer for Implantable Medical Devices
The use of a wireless resonant-energy link to energize modern implantable medical device has been suggested in [58]–[61]. More specifically, [59] presents a WPT link for powering pacemakers. The proposed system consists of two inductively coupled planar resonators and has been optimized for operation in the Medical Device Radiocommunications Service core band centered at 403 MHz. The implantable receiver is a compact, square split-ring resonator [see in Figure 18(a)], while the transmitter is a spiral loop loaded by a lumped capacitor [see the inset of Figure 18(b)]. The performance of the WPT link was experimentally investigated by using the setup illustrated in Figure 18(b); minced pork was used to simulate the presence of human tissues. The measured two-port scattering parameters are illustrated in Figure 18(c); from experimental tests, a power transfer efficiency of 5.24% is demonstrated at a distance of 10 mm.

Frequency-Agile Systems for Near-Field Deployments
Near-field WPT can be operated either at a fixed frequency, as considered in [49] (and, in this case, the optimal load value is dependent on the coupling), or with an agile frequency. In fact, when the coupling is changed, by appropriately changing the operating frequency, we can obtain higher power values on the load. The latter operating principle has been considered in [62] and [63], where a Royer oscillator was used.

Design of Nonstandard Inductive Wireless Power Configurations and the Potential Applications

Recent advances in battery and super-capacitor technology and the further miniaturization of embedded hardware have enabled the integration of inductive WPT (IWPT) in contemporary smart electronic devices [64]. At the same time, a number of industrial standardization actions and regulations have been established: the Qi standard of the Wireless Power Consortium has been defined [65], while the Power Matters Alliance merged with the Alliance for Wireless Power [66]. The name of this new alliance will be published later this year. The current state of the art for consumer electronics is oriented toward low power transfer (i.e., up to 15 W) and a well-defined alignment of the receiving structure with regard to the transmitting coil for a certain amount of time in inductive coupled systems.

Due to the basic principle of wireless inductive power transfer, it is possible to realize configurations with on-the-fly energizing of moving receivers and situations with random separations and orientations between the receiver and transmitter. However, these require further research toward an optimal design. As a representative example for moving receivers, the research group DraMCo of KU Leuven, Belgium, has investigated the inductive charging of a wireless mouse [67] of type M705 from Logitech [68], which is normally powered by two AA batteries. The available amount of space for the receiver circuitry, receiver coil, and super-capacitors was created by removing the two AA batteries. Careful design led to a solution that functions autonomously for more than 15 min, while the full charging takes only 10 s. The required time to activate the transmitter to the high-power mode is only 50 ms. Strategic placement of the transmitting structure led to an autonomous system in which regular replacement of batteries is longer no needed.

Another example is the realization of a through-display wireless charging solution for a medical wristband [69]. This device was developed for use by medical staff in maternity hospitals. It performs measurements of the body temperature, bilirubin levels, and oxygen saturation of newborn babies in only 1.25 s by means of self-designed measurement techniques. Ease of use was a key factor in the design, resulting in a device without controls. It relies on a super-capacitor energy buffer that can be charged wirelessly in fewer than 5 s by touching a transmitting unit. Through-display powering was realized by placing the receiver coil behind the display. In addition, an energy study was carried out, revealing that a full buffer provides enough energy for 38 parameter measurements or more than three days of standby time. After each measurement, the device automatically transmits the data wirelessly to a computer. The miniaturized device consists of seven PCBs and contains solely Texas Instruments

ICs (17 pieces). It is equipped with a Qi receiver, a super-capacitor charger, three power supplies, and a state-of-the-art ferroelectric random access memory microcontroller that controls the sensors, the display, the wireless transmitter, and even its own power supplies. This solution of KU Leuven was the winner of the Texas Instruments Analog Design Contest Europe 2014, among 299 submitted projects. Figure 19 shows the developed device.

Other current research projects include IoT WPT for animals, specifically to provide the energy for WSNs to monitor the health of dairy cows. KU Leuven and Ghent University recently initiated a project to construct a WSN providing real-time information on the health status of each individual cow as a member of a large stock, both indoors and outdoors. Available solutions
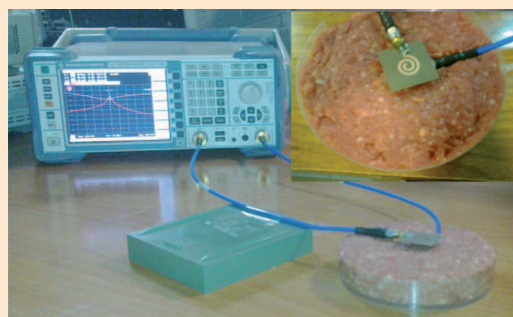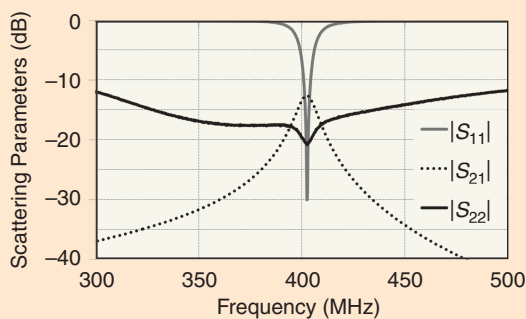
Figure 18. *The WPT link for implantable pacemakers proposed in [59]. (a) A photo comparing the receiver of the WPT link proposed in [59] and a single-chamber non-rate-responsive Discovery II pacemaker (model 481) by Guidant. (b) The experimental setup adopted for scattering-parameter measurements. (c) The measured scattering parameters.*
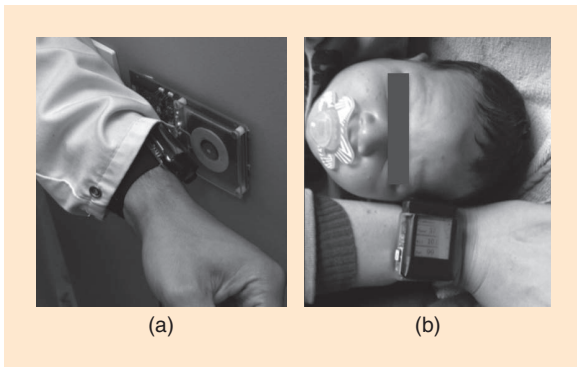
Figure 19. *User-friendly, through-display charging of a medical wristband and its autonomous functionality: (a) the charging of the device and (b) the performance of a measurement.*
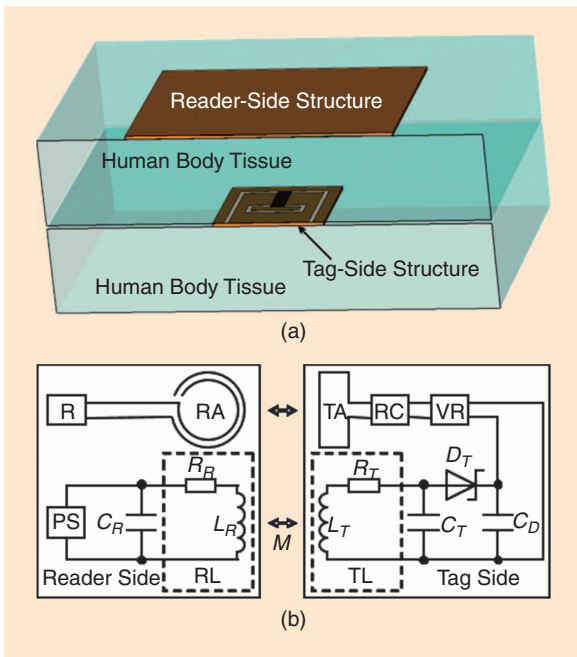

Figure 20. *(a) A cross section of a mutual arrangement of reader-side and tag-side structures. (b) The system scheme. R: reader; RA: reader antenna; TA: tag antenna; RC: RFID chip; VR: voltage regulator; PS: power source; RL: reader loop; TL: tag loop.*

for this kind of configuration consists of onboard battery-powered hardware [70]; regular replacement of the battery hinders the widespread application of this wireless solution. The goal of the project is to make use of specific and regular time slots (e.g., the animal's drinking) to wirelessly charge a super-capacitor integrated in a small, collar-attached box—thus leading to a maintenance-free technology. The energy stored on the super-capacitors can then be used for longer-haul wireless communications and powering the animal's wireless body-sensor network. Aspects such as the distance between the drinking troughs, the time the animal typically needs to drink, and the energy consumption during autonomous operation determine the design space for this inductive wireless power solution. This work is supported by the iMinds-Moni-Cow project (cofunded by iMinds, a research institute founded by the Flemish Government in 2004) and the involved companies and institutions.

Implantable, Inductively Powered UHF RFID Tag

This section provides a short overview of the development of a system design for a humanbody implant with a UHF RFID tag powered by IWPT. More details about the design can be found in [71a].

A classic RFID tag is usually passive, and its operation is enabled by power received from an RFID reader during communication [71]. However, in the case of the implantable tag, the power emitted by the reader at 866 MHz in the UHF frequency band is dissipated in the human body tissue. Increasing thickness of the tissue between the reader and the tag leads to a decrease in the tag's sensitivity for communication due to an insufficient level of power for tag operation. The problem can be overcome with the help of a tag using a semiactive chip. Powering this kind of chip can be assured not only by the reader but also by an additional source. In this case, the additional source delivering power by IWPT [72] at 6.78 MHz in the industrial, scientific, and medical (ISM) frequency band is considered.

Figure 20(a) and (b) shows the mutual arrangement and scheme of the side of the reader and the side of the tag, respectively. The elements for RFID communication and powering through IWPT on the side of the reader are designed as a center-excised Archimedes spiral antenna and a circular loop, respectively [see Figure 21(a)]. These elements on the side of the tag are represented by a folded dipole antenna and a rectangular loop [see Figure 21(b)]. Additional circuits are connected between the powering pins of the tag's RFID chip and the rectangular loop as well as to the circular loop to assure efficient powering.

The structure of the reader side is designed to be placed on the surface of the human body. The structure of the tag side is compact and suitable for implantation into the human body. The communication sensitivity of the tag is increased by 21 dB with the help of IWPT.

WPT Underwater

Today, deploying sensors in underwater environments is standard practice in several fields of activity, such as environmental monitoring aimed at collecting data on water or seabed parameters as well as to inspect permanent subsea infrastructures. These sensors may be located in fixed or mobile structures. Sensors deployed on permanent subsea structures or on the seabed generally lack cabled connections and therefore rely on batteries. Approaching these sensors with
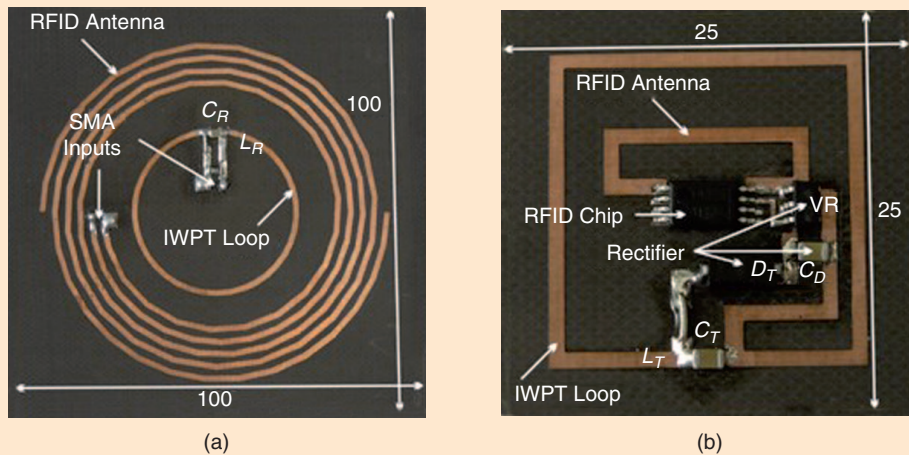
Figure 21. *(a) The reader-side structure and (b) the tag-side structure. Dimensions are in millimeters. Properties of substrate: $\varepsilon_r = 3.00$, $\tan(\delta) = 0.0014$, $h = 0.76$ mm. SMA: subminiature version A.*

autonomous underwater vehicles (AUVs) to replenish their batteries and recover measurement data is very appealing. However, presently the most common solution involves the operation of remotely operated vehicles (ROVs), which is very expensive because a support vessel is required; therefore, this can be considered only for small-scale operations. On the other hand, sensors may be carried by mobile underwater vehicles such as ROVs or AUVs for underwater sensing in specific missions. In fact, the deployment of AUVs is an emerging practice, potentially suitable for large-scale autonomous operation [72], [80]. Figure 22 shows the MARES AUV, a highly flexible, small-scale AUV, developed at the Institute for Systems and Computer Engineering, Technology, and Science (INESC TEC), that can operate at a maximum depth of 100 m and be configured to carry specific prototypes and logging systems for experimental evaluation [73].

The use of AUVs is limited by the duration of their energy-source charge. Therefore, there is a need for an energy solution that can support the operation of a number of AUVs within underwater environments for long periods of time. Currently available AUV recharging solutions are very complex, typically requiring so-called wet-mate connectors [74], which are prone to failure and require frequent maintenance and/or overly complex docking mechanisms. As such, these solutions are not appropriate for scaling up due to the high costs; therefore, their use has been limited. Research on techniques for underwater WPT has been growing over the past few years, targeting not only the battery charging of AUVs but also wireless powering of underwater sensors.

Witricity released a white paper in 2013 [75] demonstrating the possibility of using resonant magnetic coupling through salt water. The authors transferred power across a plastic container filled with water and used a halogen lamp as a load. They concluded that a significant power level (up to several kilowatts) may be transferred across a gap of 15 cm with wireless transfer efficiency in the order of 80%. Inductive coupling is currently the alternative to wet-mate connectors most often seen in the literature.

For instance, the authors of [76] describe an underwater WPT system based on inductive coupling. The efficiency and power transfer capability reported are very good, 90% and 400 W, respectively. However, the operating distance is extremely small, 2 mm. This means that there is no margin for error in terms of alignment in the AUV charging scenario. This is also the reason that in these cases some kind of mechanical stabilization is usually required. For instance, in [77] the charging station is outfitted with cones. In [78], an underwater WPT system is reported with wireless transfer efficiency of 60% across a gap of 10 cm using an antenna 25 cm × 25 cm in size. The authors state that the energy flow in seawater is guided by eddy currents caused by the magnetic field (although the power level is not mentioned). A novel WPT technique that considers the coupling
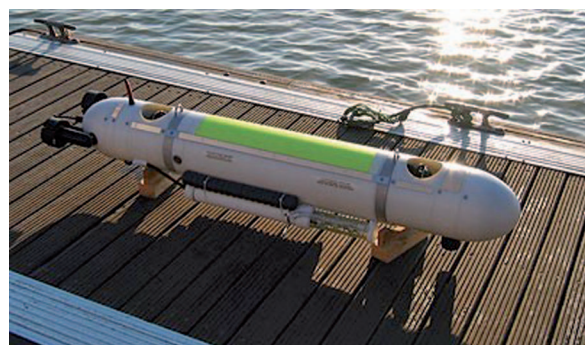

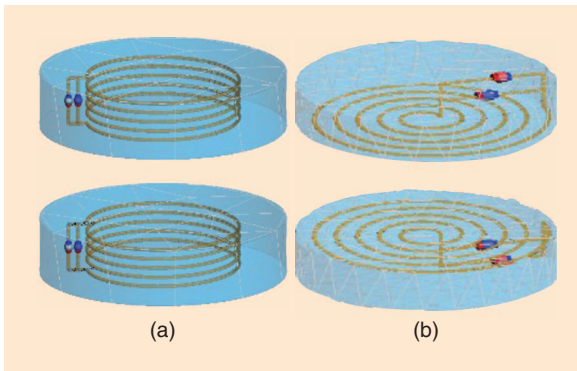**Figure 22.** *The MARES AUV developed at INESC TEC.*

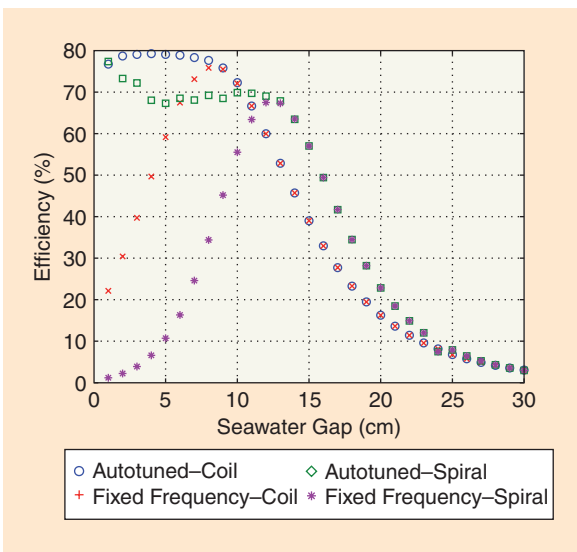**Figure 23.** *Two underwater WPT simulation models: (a) a coil-based inductor and (b) a spiral-based inductor.*

Figure 24. *The efficiency versus seawater gap for both configurations shown in Figure 23.*
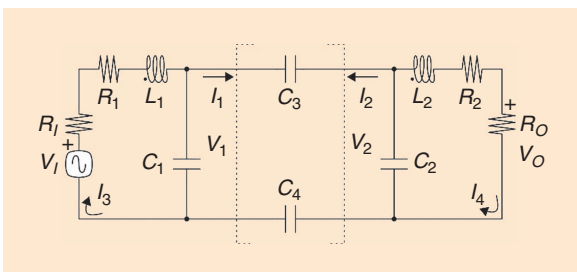

Figure 25. *The circuit model considered in studying REC.*

both having a maximum diameter of 16 cm and 3 mm of copper thickness. In both cases, a parallel capacitor was included to achieve antiresonance at around 100 kHz, where the system operates optimally using 50-Ω impedance at both the transmitter and load sides.

Seawater was considered as the transfer medium (permittivity of 81 and conductivity of 4 S/m), while the transmitter and receiver where kept in a box filled with distilled water to avoid resonance losses. A third configuration based on parallel plates was evaluated to assess the viability of the REC principle for underwater WPT. However, the conductivity of the transfer medium was observed to dramatically reduce the efficiency of the method, rendering it useless even at very short ranges.

The simulated efficiency as a function of the seawater gap is presented in Figure 24. As can be seen, the efficiency remains approximately constant in the overcoupled region, up to 8 cm and 13 cm, for the coil-based and spiral-based inductors, respectively. Efficiency falls rapidly after that point, corresponding to the undercoupled region. Depending on the requirements of the problem at hand, any of the solutions may be attractive. Underwater WPT using magnetic resonance appears to be a promising solution to transfer power to underwater equipment.

REC in WPT

The wireless transfer of power based on electrical resonance mentioned in the previous section is based on the circuit model shown in Figure 25. In this circuit, power is wirelessly transferred from the source (on the left) to the load (on the right) through the capacitances C3 and C4. The resonances at the transmitter and the receiver are defined by L1 and C1 and by L2 and C2, respectively. As shown in [81], a very reasonable efficiency can be achieved with very low values of C3 and C4, as long as the losses, represented by R1 and R2, are kept low. This is similar to resonant magnetic coupling in the sense that very reasonable efficiencies can be achieved with very low magnetic coupling coefficients if the losses are kept low. Low values of C3 and C4 and low magnetic coupling coefficients are extremely important to the increase of spatial freedom. Spatial freedom is currently one of the most desirable properties in WPT.

An implementation of the circuit in Figure 25, consisting of two identical devices, is shown in Figure 26. Each device measures approximately 16 cm × 16 cm × 3.6 cm and is composed of a coil and two conductive plates identical in area. The capacitances C1 and C2 are implemented by the close proximity of the conductive plates in each device. Figure 27 shows the voltage measured at the terminals of a 680-Ω load connected to the output of an RF–dc converter. As shown in Figure 26, the RF–dc converter is connected to one of the devices, with the other device connected to a signal generator.

through the electric field rather than from the magnetic field is resonant electrical coupling (REC), which was independently proposed by [79] and [80] in 2014. However, deployment of REC for underwater WPT has not yet been reported.

The following discusses the results from an underwater WPT system evaluation using three-dimensional (3-D) electromagnetic simulation. As shown in Figure 23, we consider two different architectures: a coil-based and a spiral-based copper inductor setup,

At this point, experimental peak efficiencies of 61% and 38% can be obtained at distances of 12 cm and 30 cm, respectively.

It is also possible to observe a relatively low variation of peak voltage in the case of a rotational misalignment, in particular when the receiver is perpendicular to the transmitter, as shown in Figure 28. However, it is important to note that this behavior is most likely caused by the constructive combination of REC and resonant magnetic coupling addressed in [82], rather than REC alone.

WPT Applications

WPT Integration in Buildings

The physical layer is crucial for the effective integration of the electronics with any hosting object. Mechanical flexibility, high shape customization, recyclability, and low fabrication-process and materials costs are needed to enable the IoT. For these reasons, particular attention has to be given by the scientific community to demonstrating substrate-independent processes that make possible the application of the devices on many materials, especially those not normally used in electronics [85]. Common substrate-independent processes that fit these requirements include inkjet printing [7], 3-D printing, gravure printing, screen printing, and metal adhesive laminate [86], [87].

As a case of study, we consider so-called energy evaporation, a system in which localization capabilities in conjunction with long- and short-range WPT functionalities are combined and embedded into floors [88]. This example is significant because it shows the need for integration between large-area electronic devices and the environment.

Figure 29(a) shows the scheme of a distributed matrix of unit cells composed of a 5.8-GHz patch antenna surrounded by a high-frequency coil at 13.56 MHz. The patch is responsible for long-range WPT, while the coil has the dual role of short-distance WPT source and localization through connection with near-field communication tags. In Figure 29(b), the performance of the unit cell fabricated on top of a cork substrate demonstrates the scheme's feasibility, adopting a material that is unconventional for electronics (but common in indoor environments). The fabrication was performed using a metal adhesive method [87].

The importance of the result shown in Figure 29 is its demonstration that, if properly designed, RFID tags and RFID sensors could be integrated in tiles and similar construction materials, thus enabling a variety of novel energy-autonomous IoT and WPT applications.

Algorithmic WPT Applications in Wireless Ad Hoc Networks

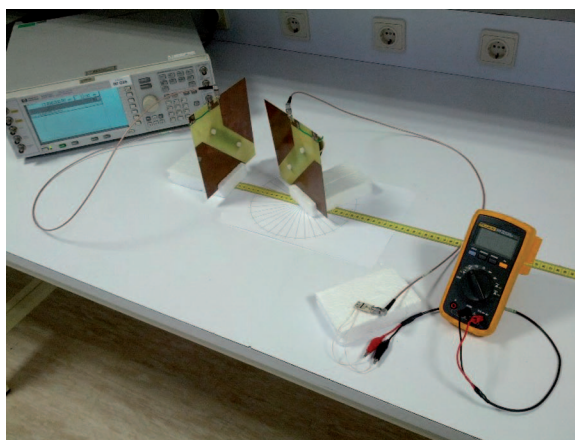WPT technologies offer new possibilities for managing the available energy and lead the way toward a

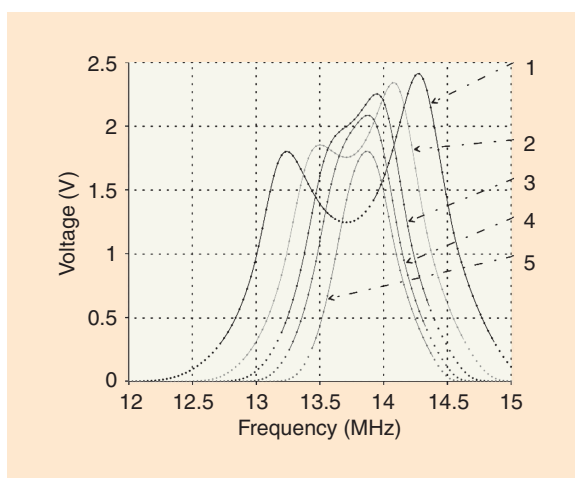**Figure 26.** *The prototype used in the experimental validation of REC.*

Figure 27. *The measured voltage as a function of frequency for distances equal to 12 cm (curve 1), 16 cm, 20 cm, 24 cm, and 30 cm (curve 5), considering a transmitted power of 16 dBm.*
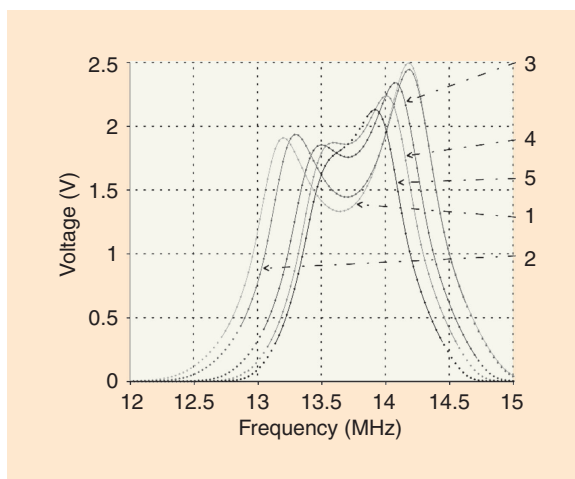

Figure 28. *The measured voltage as a function of frequency for angles equal to −90° (curve 1), −40°, 0° (the same as in Figure 27), 40°, and 90° (curve 5), considering a transmitted power of 16 dBm and a distance of 16 cm.*
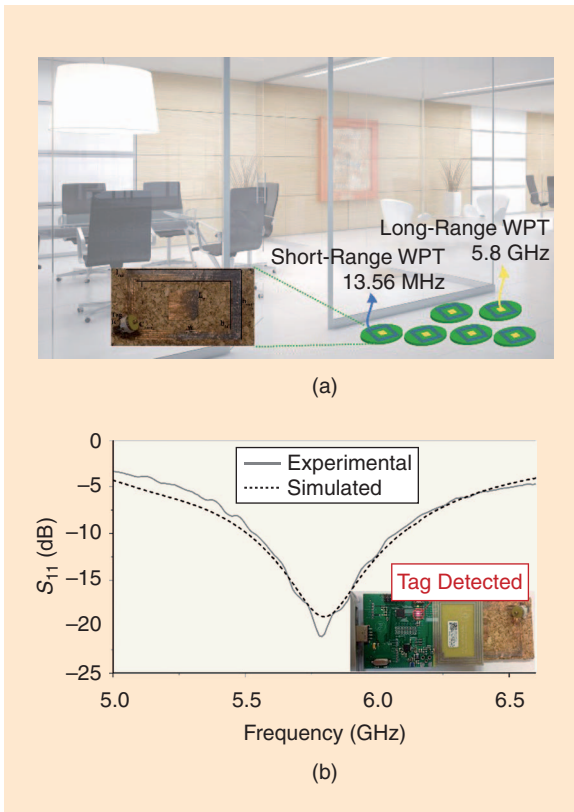
Figure 29. *Energy evaporation: (a) an illustration of the concept and (b) the performance of a unit cell fabricated on cork. Based on [86].*

new paradigm for wireless ad hoc networking [89]. WPT-enabled networks consist of nodes that may be either stationary or mobile, as well as a few mobile nodes with high energy supplies [90]. The latter, by using WPT technologies, are capable of quickly recharging the network nodes. In this way, the highly constrained resource of energy can be managed very precisely and efficiently. Another important aspect is that energy management can be performed passively from the perspective of nodes and without the computational and communication overhead introduced

Figure 30. *The layout of an experimental setting for WPT in wireless ad hoc networks.*

by complex energy-management algorithms. Finally, energy management can be studied and designed independently of the underlying routing mechanism used for data propagation.

There are considerable challenges in making such wireless-power-enabled ad hoc networks work. First, the control of wireless chargers, whether stationary or mobile, is not trivial. Assuming a finite initial energy, these devices have a limited lifetime, so their available energy supplies should be injected into the network wisely. Second, the WPT process is, in itself, a challenging task. For example, the extent to which a network node should be charged to prolong the global network's lifetime is not obvious. Finally, other issues such as the amount of energy given to the chargers, the trajectory they should follow inside the network, and their behavior with respect to the communication pattern and the energy dissipation inside the network further complicate the design and implementation of a wireless ad hoc network of this kind. An example layout of a proof-of-concept setting for WPT in wireless ad hoc networks is shown in Figure 30.

The charging process's impact on the network's lifetime is studied in [91] for selected routing protocols. Following a detailed experimental evaluation, a mobile charging protocol that locally adapts the circular trajectory of the mobile charger to the energy dissipation rate of each network subregion is proposed and compared against several other trajectories. The derived findings demonstrate significant performance gains in uniform network deployments.

The authors of [92] propose three alternative protocols for efficient recharging, addressing key issues identified as 1) the extent to which each sensor should be recharged, 2) the best split of the total energy between the charger and the sensors, and 3) the optimal trajectories the mobile charger should follow. One of the protocols performs some limited, distributed sampling of the network status; another reactively adapts to energy shortage alerts judiciously spread across the network. As detailed simulations demonstrate, both protocols significantly outperform known state-of-the-art methods and get quite close to the performance of the global knowledge method, which is also discussed, especially in heterogeneous network deployments.

The idea of deploying multiple mobile chargers in a network is investigated in [93]. Here, four new protocols for efficient recharging are proposed, addressing optimal coordination procedures and good trajectories for mobile chargers. Two of the protocols perform limited, distributed network knowledge coordination and charging, while two others perform centralized global network knowledge coordination and charging. As detailed simulations demonstrate, one of the distributed protocols outperforms a known state-of-the art-method [93a], while its performance gets quite close

to the performance of the powerful centralized global knowledge method.

The collaborative charging feature is enhanced in [94] by forming a hierarchical structure. Two types of chargers are distinguished: hierarchically lower mobile chargers, which charge sensor nodes, and hierarchically higher special chargers, which charge the mobile chargers. Four new collaborative charging protocols are designed and implemented to achieve efficient charging and improve important network properties. The protocols are either centralized or distributed and assume different levels of network knowledge. Extensive simulation findings demonstrate significant performance gains with respect to noncollaborative state-of-the-art charging methods. In particular, the protocols improve several network properties and metrics, such as network lifetime, routing robustness, coverage, and connectivity. A useful feature of these methods is that they can be suitably added on top of noncollaborative protocols to further enhance their performance.

In [95], another approach is followed to study the problem of efficiently charging a set of rechargeable nodes using a set of wireless energy chargers, imposing safety constraints on the electromagnetic radiation incurred. A new charging model is defined that differs greatly from existing models in that it takes into account real technology restrictions on the chargers and system nodes, mainly regarding energy limitations. The model also introduces nonlinear constraints (in the time domain) that radically change the nature of the computational problems considered. In this charging model, the low-radiation efficient charging (LREC) problem is presented and studied; here, the amount of "useful" energy transferred from chargers to nodes (under constraints on the maximum level of imposed radiation) is optimized. Several fundamental properties of this problem are presented, and indications of its difficulty are shown. Finally, an iterative local improvement heuristic for LREC is proposed, which runs in polynomial time and the performance of which is evaluated via simulation. The algorithm decouples the computation of the objective function from the computation of the maximum radiation and also does not depend on the exact formula used for the computation of the electromagnetic radiation in each point of the network, thus achieving good tradeoffs between charging efficiency and radiation control. In addition, the algorithm exhibits good energy balance properties. Extensive simulation results supporting the claims and theoretical results are provided [95].

In [96], wireless power transmitters that charge the battery of the network nodes in mobile ad hoc networks are employed, and two new alternative protocols that configure the activity of the chargers are proposed. One protocol performs wireless charging focused on charging efficiency, while the other aims at a proper balance of the transmitter's residual energy. Toward a more realistic validation, an evaluation is performed not in a simulation environment but through an experimental setting of real devices. Figure 30 shows the layout of the experimental setting in which four wireless power transmitters and three wireless sensor motes were used.

Solution of WPT for Spatially Distributed Nodes of WSNs

WSNs based on the ZigBee protocol, for example, are low-power, low-throughput networks commonly used for distributed low-range sensing and control. In some cases, spatially distributed ZigBee nodes cannot be powered up using batteries or cables. In these cases, an RF-based WPT system can be considered a potential solution. Because demand on power for each WSN node can vary over time, the charging system must constantly monitor the state of each node and send an adequate amount of energy to allow constant operation. Examples of other WPT schemes for WSNs can be found in [96] and [97].

This work presents a concept and physical realization of a 2.45-GHz WPT system for charging WSN nodes that are spatially distributed. The system utilizes a 4×1 patch-array transmitter with a switched radiation beam to ensure large spatial coverage. The beamswitching is realized using a 4×4 Butler matrix, the inputs of which are connected to an SP4T four-way high-isolation RF switch. After connecting the switch to the high-power signal generator (here, a WSN node generating a single-tone, 2.45-GHz signal along with a 1-W amplifier for each Butler matrix input to increase the power level), a directional transmitter was obtained. On the receiving side, the RF power was collected using a highly directional planar Yagi-Uda antenna. The antenna was connected to a rectifier including a five-stage voltage multiplier and a matching circuit for a high dc output level. The output of the rectifier was connected to the 0.47-F super-capacitor gathering energy for powering one WSN node. In total, four receivers were used in the proposed system, each placed in the maximum gain direction of each transmitter radiation pattern. The schematic drawing of the system is shown in Figure 31.

During the operation of a WSN node, measurements of certain physical quantities can be completed (by a WSN in the receiver site in Figure 31) and sent to the data sink. Apart from that, each WSN node can measure and send the voltage level of the super-capacitor to which it is connected. The voltage levels can be collected periodically from each WSN node to the data sink located at the transmitter. Based on WSN node responses, the transmitter radiation pattern can be autonomously switched in time to cover current energy demand of each WSN node and thus allow the network to remain operational for a long time.
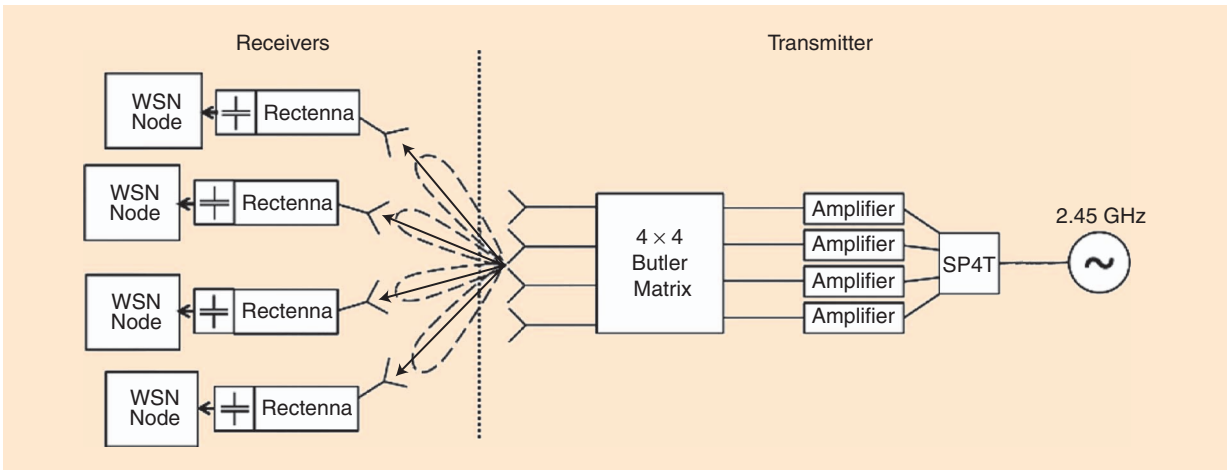
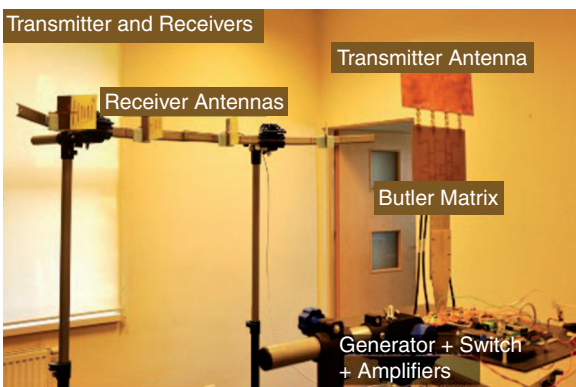**Figure 31.** *The schematic of the proposed WPT system.*

Figure 32. *An autonomous WPT system realized for supplying power to WSN nodes distributed in space.*
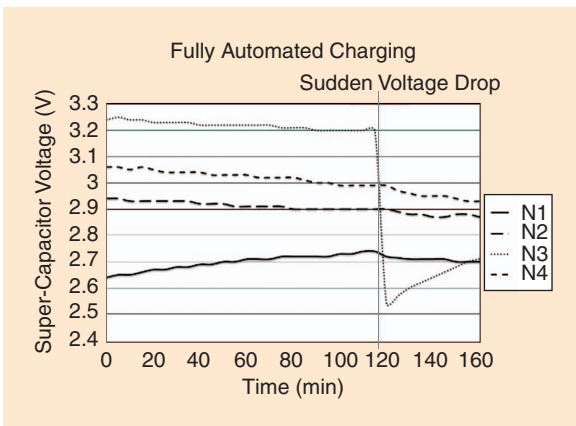

Figure 33. *The results of the charging experiment for the example system shown in Figure 32.*

Using received voltage levels, the transmitter can switch radiation patterns according to the following algorithm:

1) Receive voltage levels from all nodes.

2) Calculate difference and offset from the limit voltage value for each node.

3) Calculate illumination duration for each node, i.e., the weighted sum of factors from point 2).

4) Start counter and switch radiation patterns in calculated moments.

5) Go to point 1).

Figure 32 shows a WPT system for automated charging of WSN nodes. To verify performance of the WPT system, a charging experiment was performed. In the experiment, all WSN nodes both measured and sent data to the sink while being charged according to the algorithm. Voltage levels measured by all WSN nodes versus time are presented in Figure 33.

As can be seen, the node with the lowest voltage level obtains the highest amount of energy from the transmitter. Other nodes discharge slowly, but in case of high energy loss (the sudden voltage drop shown in Figure 33), the system would direct the energy flow to the nodes most in need of energy.

The presented 2.45-GHz WPT system allows wireless charging of multiple WPT nodes by switching the transmitter's radiation pattern. The implemented algorithm allows full automation of the charging process and also equalization of voltage levels for all WSN nodes, independent of the node's measurement frequency and initial voltage level.

Exploitation of 3-D Textile Materials for Wireless Feeding of In-Car Sensor Networks

The 3-D textile material shown in Figure 34 consists of two firm layers at a constant distance. The distance between the layers is kept constant by fine fibers perpendicular to the firm layers. Hence, the 3-D fabric can be understood as a dielectric waveguide. This 3-D fabric can be used as upholstery in cars, buses, or airplanes, and such upholstery can play the role of a feeder or a communication channel.

The idea of exploiting a 3-D textile material for a WPT was tested in a car with a metallic roof (Figure 35). The transmit antenna and receive antenna were attached to a 3-D textile upholstery. Using this technique, the electromagnetic energy was efficiently guided by the textile material along the car roof.

The idea was verified by measurements in a real car. In Figure 36, the transmission between antennas in free space (black) is compared with the transmission between antennas placed on the roof upholstery of an empty car (blue) and a fully occupied car (red). The efficiency of the described WPT is demonstrated in Figure 37, which compares transmission between the transmit antenna and the receive antenna placed in free space (black), on conventional upholstery (blue), on 3-D textile (green), and in 3-D textile (red).

To minimize attenuation of the channel, the transmitted electromagnetic wave must be polarized perpendicularly to the metallic surface of the roof. Therefore, an open-ended rectangular waveguide and a planar horn antenna integrated to the substrate were used in the experiments (Figure 38).

For experiments in a car, the planar horn antenna integrated to the substrate showed better behavior, thanks to its narrower radiation pattern (Figure 39). For measurements in the laboratory, the open-ended rectangular waveguide was exploited due to a simpler calibration.

Harmonic Tags

In the field of passive UHF RFID, the nonlinear behavior of the harvesting section of the RFID chip can be exploited to develop augmented tags. Three categories of applications can be envisaged by exploiting 1) the impedance power dependency [101], [102], 2) harmonic generation [103]–[105], and 3) efficient waveform design [106]–[108].

To enable such applications, the nonlinear characteristics of the RFID chip must be determined. Figure 40 shows the normalized power spectral density of
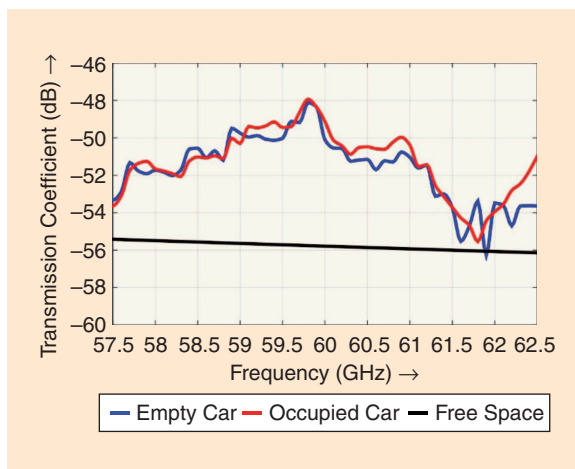

Figure 34. *The 3-D textile material.*

Figure 35. *An experimental radio link that runs along the roof of a vehicle using a 3-D textile upholstery. Rx: receive; Tx: transmit.*

Figure 36. *The transmission between SIW horn antennas fixed on 3-D textile upholstery on the roof of a car.*
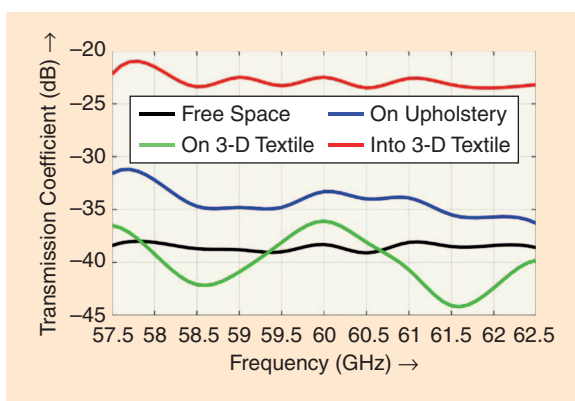

Figure 37. *The transmission between antennas over a distance of 180 mm in free space (black), on conventional upholstery (blue), on 3-D textile (green) and in 3-D textile (red).*

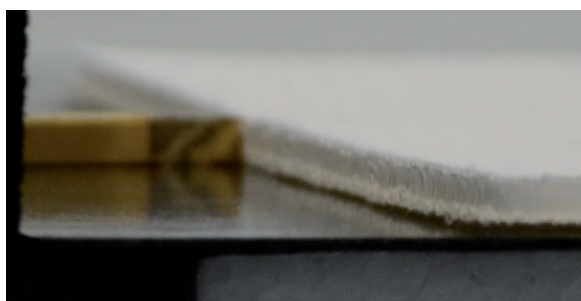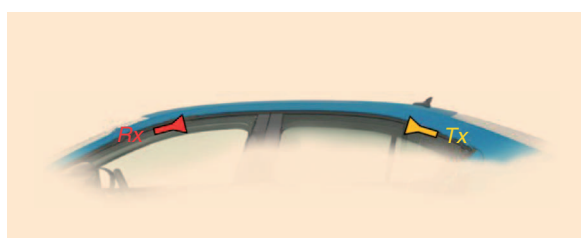**Figure 38.** *(a) The planar horn antenna integrated to a substrate and (b) the open-ended rectangular waveguide.*
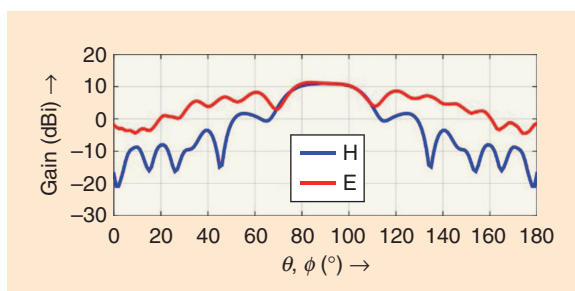

Figure 39. *The directivity patterns of the planar horn antenna integrated to substrate in the E plane (red) and H plane (blue).*

a passive RFID chip response measured using a similar method to the one reported in [104]. The setup considers the chip activation threshold power, the reader harmonics suppression, and the chip impedance matching at the fundamental frequency as in common tags. The harmonic frequency level (i.e., at 1.736 GHz and, notably, at 2.604 GHz) at the chip activation threshold is significant compared to the fundamental frequency level. The energy contained in the third harmonic generated by the RFID chip can be exploited to set a second RF tag-to-reader link at that harmonic frequency.

Harmonic Tag Design
A proper design of the tag antenna enables the transmission of the modulated third harmonic signal from tag to reader [102]. The obtained channel diversity can be exploited as a redundant communication channel, e.g., to increase the robustness of the RF uplink. Additionally, the pattern direction of the antenna can be designed to be different than the one for the fundamental signal, e.g., to develop an application for localization. It can also be used to enable some specific applications by receiving the signal at the third harmonic.

Measurement
Figure 41 shows an example of a harmonic tag using a dual-band, low-frequency inverted antenna. Figure 42 shows the third order harmonic response levels of two prototypes based on the harmonic tag with a different chip in each one (chip 1 [108] and chip 2 [109]) and one commercial tag. The results of an experimental parametric analysis are summarized in Table 2.
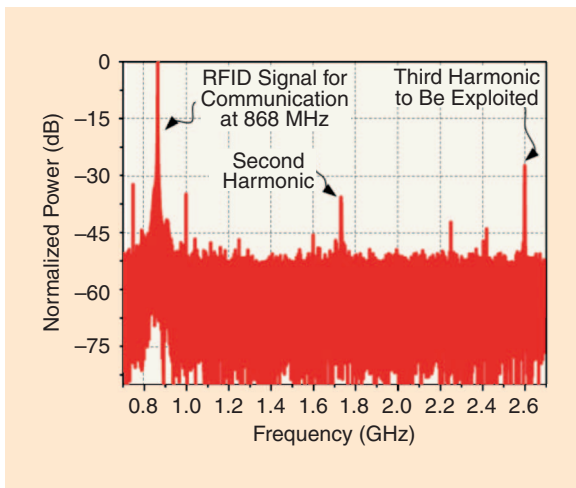

Figure 40. *An example of the normalized power spectral density of a tag response measured at the activation threshold of the chip under test.*

Figure 41. *An example of a harmonic tag. It communicates at the fundamental frequency and third harmonic. The RFID chip is connected to the dual band antenna with appropriate matching sections.*

Figure 42. *The isotropic received power of the harmonic tag response at the third harmonic in function of the EIRP transmitted by the reader. The measured power considers an isotropic antenna at reception in a bistatic configuration with 1-m distance between the reader and tag.*

TABLE 2. Parametric analysis results.			
	Frequency	**Power of the Response at 3f**	**Read Range at the Third Harmonic***
Fabrication sensitivity	12-MHz detuning	−82 dBm	High dependency
Kind of chip	Greater bandwidth with chip 1	Quasi-similar for both chips	3.5 m for chip 2 3.0 m for chip 1
Commercial tag	Slightly wider bandwidth for commercial tag	−90 dBm	Lower than 1.5 m

* The read range at $3f_0$ considers −90 dBm of reader sensitivity.

Figure 43. *A block diagram of the RFID-enabled LMS. LAN: local-area network.*

As can be seen in Table 1, the read range at the third harmonic is a few meters, which is comparable to that at fundamental frequency in this design. However, the design of the antenna at the third harmonic could be quite different to enable new applications. Localization, energy harvesting, sensing, and authentication are among the possible options.

UHF RFID Library Management System

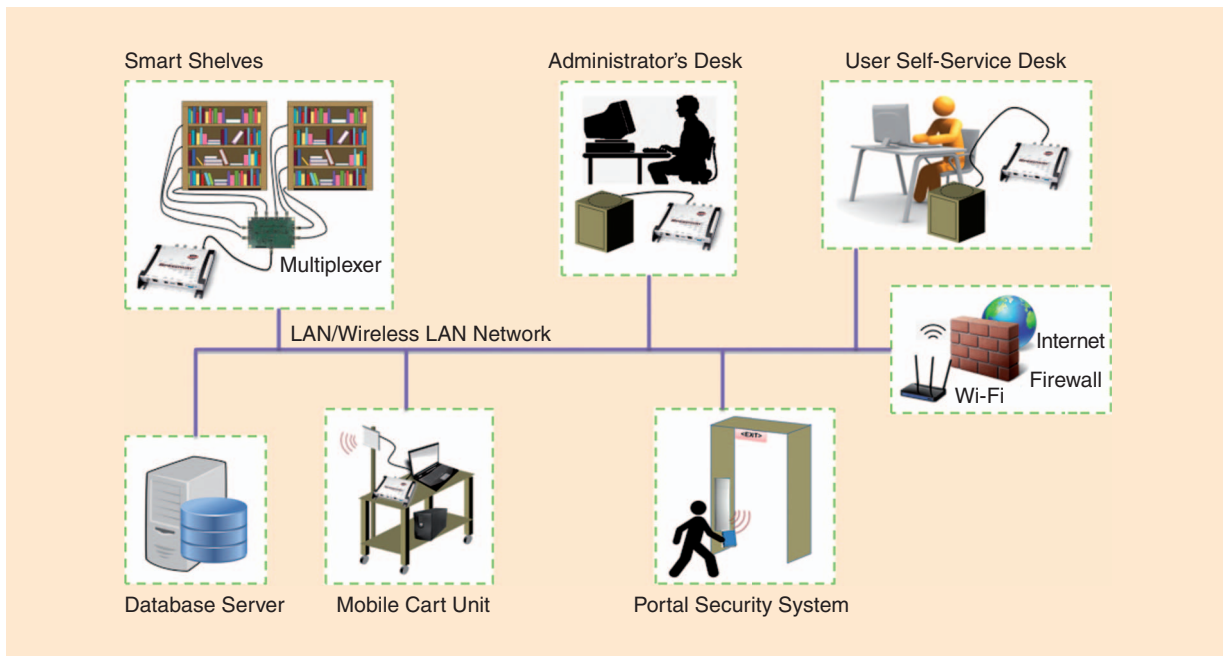A passive UHF RFID library management system (LMS) was designed and built to serve the purpose of a university library [112]. The prototype was actually built and tested in a laboratory setting with very good evaluation results. The main objectives of the project were to 1) provide stock management, including inventory monitoring, identification of missing or lost library items, and locating books on shelves; 2) implement item security measures against possible thefts often incurred in libraries; and 3) eliminate time-consuming processes when checking items out of the library or returning items to the library.

A block diagram of the RFID-enabled LMS is shown in Figure 43. It consists of several subsystems including smart shelves, a user self-service desk, a database server, a portal security system, and a mobile cart unit. The database server is the backbone for the entire system. It is the place where all the relevant information such as book titles, user accounts, checked-out books, and stock-taking reports are kept.

Using the self-service desk [see Figure 44(b)-(c)], which consists of a PC, an RFID reader, and a near-field antenna, library users can perform all functions that
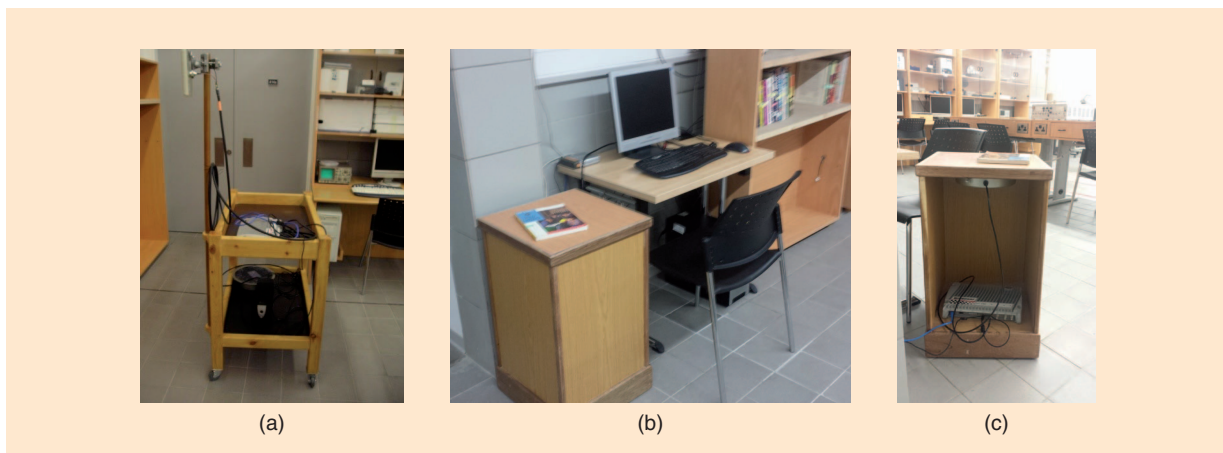

Figure 44. *(a) The mobile cart unit equipped with an RFID reader, antenna, and autonomous power supply; (b) and (c) the self check-out/in counter for library users.*

typically take place in a library environment: search for a book by title, author, publisher, or ISBN number. In addition, they are allowed to review their own activity record, self-checkout books, and return to the library previously checked-out books. A user-friendly graphical interface was developed to provide users with enhanced functionality and transparency. Through this interface, the librarian has additional privileges compared to the average user, including the ability to modify system settings, edit user accounts and book entries (e.g., add new books), take stock, and monitor the RFID entrance security system (shown in Figure 43).

The smart shelves of the LMS, depicted in Figure 45, are especially designed to serve the tasks of the university library. Each cabinet is equipped with an RFID reader with multiple ports connected through cables to each of its shelves. Although these shelves look like common shelves, they are, in fact, especially designed RFID antennas, such as the one illustrated in Figure 46, through which the reader can

Figure 45. *The prototype library cabinet with four shelves. The shelf antennas are fed on the side with coaxial cables running from the reader's ports or the multiplexer. Books (equipped with RFID tags) reside on top of the shelf antennas.*

Figure 46. *The shelf antenna with an N-type connector on the side.*

receive the unique identification numbers (electronic product code) of the books that are placed on top of them. This enables automatic stock-taking with the push of a button, as well as locating and identifying missing and misplaced books on library shelves in record time. RF multiplexers (as shown in Figure 47) are also used at intermediate points between the reader and the shelf antennas to reduce the total number of readers required to cover the overall needs of the library. The multiplexers are software-controlled (using Arduinos), and they are already implemented in the in-house developed software application. Each RFID reader can be connected and service up to 32 antennas.

A security portal at the entrance of the library, as shown in Figure 43, consists of a stationary RFID reader and a high-gain antenna or array of antennas. This system is connected to the network to provide access to the software application developed for this purpose. Alert information is passed to a dedicated software application that runs on the circulation desktop, which is controlled by the library administrator. The system is programmed to activate an alarm every time a nonauthorized attempt is made to remove library items (e.g., books and magazines) from the library entrance.

A mobile cart unit, shown in Figure 44(a), enables book identification and localization on the library shelves. The mobile cart system is equipped with an RFID reader, an antenna, a laptop/tablet with touch screen, and a UPS that provides power to the reader and laptop. The system uses the Wi-Fi connection to access the database server and provide valuable information to the user. The mobile cart can be pushed around the library while scanning the books on individual shelves.

The ability of the system to effectively read and correctly identify the books residing on top of the shelf antenna depends on the electromagnetic coverage, the uniformity and strength of the field in the volume of the shelf, and the interference to nearby shelves. It was identified experimentally that tag readability requires a minimum field level of approximately 20 dBV/m [113]. The wooden cabinet that was built and tested in the laboratory was also modeled on SEMCAD-X using a FDTD algorithm [114]. Our goal was to identify problematic regions either due to reduced electromagnetic coverage or strong interference in neighboring shelves.

In Figure 48, the areas where the electric field values are above 20 dBV/m are shown in yellow for two antenna designs: a straight line and a meander line. Figure 48(a) and (b) represents the field magnitude for the straight line; Figure 48(c) and (d) represents the corresponding field for the meander line. The straight line was excited with a power source set to 20 dBm, whereas the meander line was excited with a power source at 15 dBm. It is clear that both antennas result
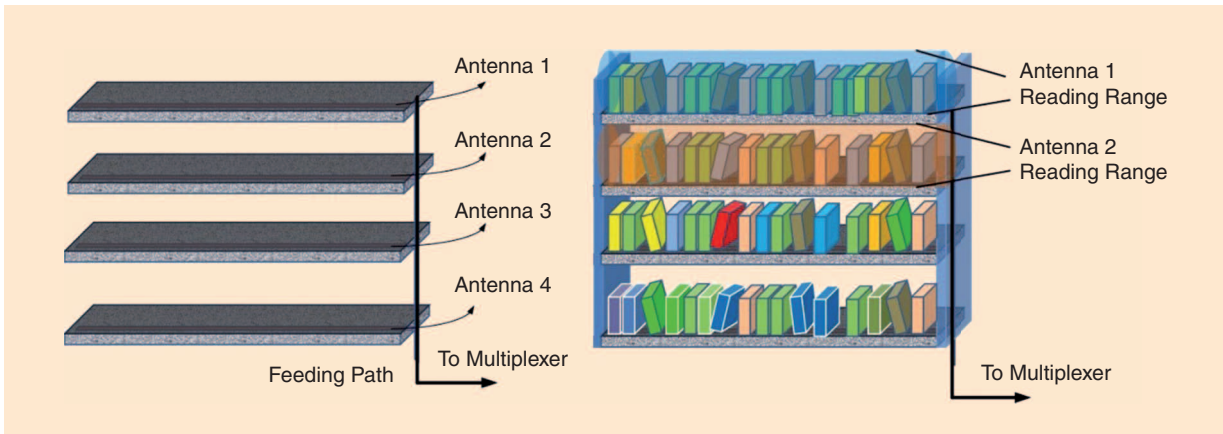
Figure 47. *The proposed library cabinet composed of four shelves. Each of the four shelf antennas is connected to an RF multiplexer output.*

in reduced electromagnetic interference for nearby shelves. However, the meander line with a lower input power level seems to provide a better electromagnetic coverage and even lower electromagnetic interference.

In addition to electromagnetic coverage and interference at nearby shelves, the distribution of the peak spatial specific absorption rate (SAR), averaged over 10 g of tissue mass ($psSAR_{10g}$), was assessed for a human model (phantom) [115] in close proximity to shelf antennas with and without the presence of books on the shelf. The dielectric properties of the human tissues were calculated according to the parametric model proposed by Gabriel et al. [114]. In the worst-case scenario, all shelf antennas in the cabinet were active. All values were normalized to 1 W of power radiated by each antenna.

In the case of the wooden cabinet and straight-line antennas, higher $psSAR_{10g}$ values were calculated when the model was placed at the shortest distance to the shelf but in the absence of books. SAR values were in all cases reduced by a factor of ten as compared to those obtained for a metallic cabinet. Specifically, at 5-mm distance, the maximum SAR values are 0.076 W/kg

for Thelonious (see Figure 49), 0.059 W/kg for Ella, and 0.041 W/kg for Duke (all these are all human models) [114]. When the human models were placed 10 cm away from the cabinet, the corresponding SAR values were reduced to 0.022 W/kg, 0.015 W/kg, and 0.012 W/kg, for Thelonious, Ella, and Duke, respectively.

WPT for Batteryless Biomedical and Implantable Microsystems

WPT is desperately needed in wearable biomedical sensors [116], implants [117], individually addressable neurostimulators [118], retinal and other prostheses [119], and biomedical applications such as interventional magnetic resonance imaging (MRI) [120]. In each of these critical applications, there is an important size constraint on a system that makes the use of batteries impractical because this limits overall size and shortens lifetime. Certain applications such as MRI have high-power internal electromagnetic fields that prohibit the use of long metallic wires due to induced heating. Therefore, power and data transmission must be done wirelessly to the systems in these applications, and they must be miniaturized.
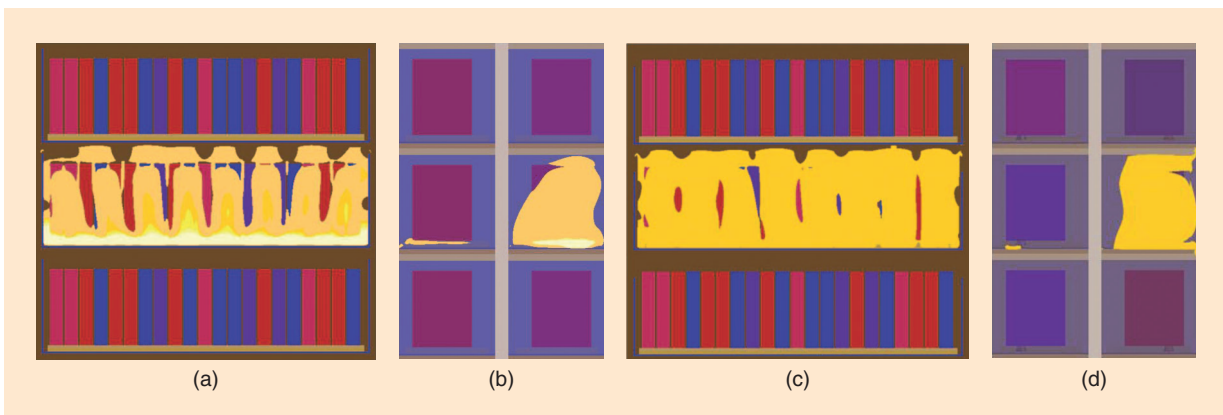

Figure 48. *Electromagnetic coverage and interference for nearby shelves. The yellow color corresponds to the magnitude of the electric field above 20 dBV/m. (a)–(b) The shelf antenna is a straight microstrip line at the bottom of the shelf; (c)–(d) the shelf antenna is a meander line at the bottom of the shelf.*
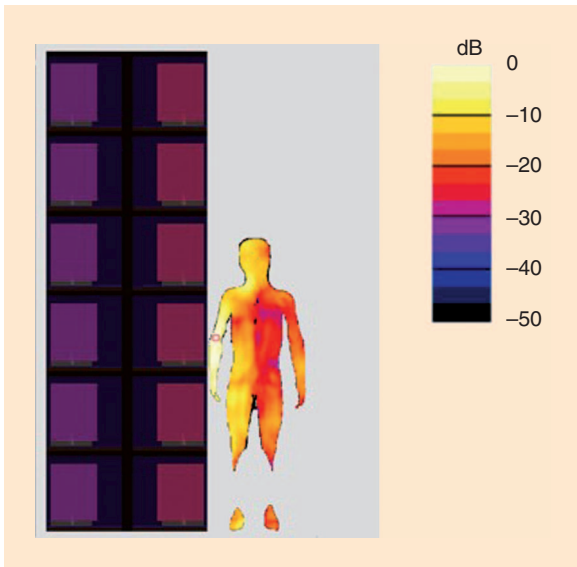
Figure 49. *Thelonious standing sideways 5 mm away from the edge of the shelf when all shelf antennas are radiating. The maximum SAR value is identified at the arm.*

In addition to transmitting data, these microsystems should also be able to receive data to be programmed or to awaken. Typically, long operation distance, higher bandwidth, and lower power densities are desired. However, meeting these in a small batteryless system is still a big design challenge, the realization of which would open a world of widely used wireless health monitoring systems.

WPT to batteryless microsystems can be achieved using inductive or capacitive coupling in the near field. Inductive coupling with the reception of modulated backscattered data is a frequently employed technology in implants and is also used commonly in passive RFID tags. This technology results in small sizes. However, it has the disadvantage of shorter operation distance of around 0.5–20 cm [121]. CardioMEMS has a passive-telemetry-based implanted wireless blood-pressure sensor system working over a distance of 20 cm with a size of 5×30 mm^2 [122]. A low megahertz region, such as 3 or 30 MHz, is found to provide a good compromise between tissue absorption and bandwidth [123]. However, research still continues to find the optimal frequency for WPT into tissue [124].

Several other biomedical implants have been proposed using this type of telemetry. However, many require large antennas because of frequency ranges in the megahertz being used. Antenna sizes are on the order of one to tens of centimeters when the gigahertz frequency range is used [125] and become greater as frequency declines. Miniaturized, wirelessly powered passive RFID tags operating at 60 GHz are shown to work with an antenna occupying a total area of 20 mm^2 [126] but at the cost of increased path losses, design complexity, and power density [127]. A biomedical implant

has been proposed using 1-GHz power for a 2×2 cm^2 square loop transmit antenna and a 2×2 mm^2 square loop receive antenna through 15 mm of layered bovine muscle tissue with a measured link gain of −33.2 dB [128]. Active microsystems can obtain better operation distance using smaller antennas or coils of around 0.5 mm; unfortunately, this means they must include batteries [129].

Optical Power Transmission for Wireless Sensors and Microsystems

In the context of system miniaturization and wireless power and data transmission, optoelectronic systems have the potential to be smaller than the RF-powering WPT solutions. They offer higher power densities that can be delivered simply by lasers or other light sources. Laser-beam powering of RF tags with on-chip silicon photodiodes has helped miniaturize them to 500 × 500 μm^2 sizes [130]. This miniaturization has proved valuable in studying ant behavior by tagging individual ants [131]. However, in these small RF tags, communication is established by RF signals using small on-chip antennas, which limits the working distance to around 5 mm.

A 1.5 mm^3 energy-autonomous wireless intraocular pressure monitoring system has been implemented using an integrated 0.07-mm^2 solar cell that can harvest a maximum power of 80 nW under a light irradiance of 100 mW/cm^2 (air mass 1.5 sun condition) to recharge a 1-mm^2 thin-film battery to power the system. It also includes a 4.7-nJ/bit frequency-shift keying (FSK) radio that achieves 10 cm of transmission range, which is also used to receive wake-up signals [132]. Another version of this microsystem is also implemented by employing an integrated optical receiver, instead of the RF receiver, to load program and request data, maintaining optical powering and RF data transmission. The system generates 456 nW under 10 kilolux light to enable energy-autonomous operation [133]. Another solution has been demonstrated for this problem with a microsystem aligned to the tip of an optical fiber, where an on-chip photovoltaic cell is used for optical powering and a separate laser diode for communication [134], [135].

Despite being very attractive solutions for WPT, on-chip photovoltaic cells made of silicon can supply open-circuit voltage of around 0.6 V, which is not enough for ICs and sensors. Series connection of multiple photodiodes in silicon-on-insulator (SOI) wafers has been demonstrated as a solution [136]; however, SOI technology is more expensive and less available compared to standard complementary–metal-oxide-semiconductor (CMOS) processes. An external light-emitting diode (LED) used as a photovoltaic cell can be more beneficial.

A LED can supply higher open-circuit voltage (1.3 V for near infrared, 1.6 V for red, 1.7 V for green, etc.)

than silicon photodiodes. Circuitry can be run directly from this higher voltage without the need for voltage elevation, which consumes valuable power. Because the microsystem needs an external optoelectronic element to transmit data optically (silicon, being an indirect semiconductor, cannot generate photons of any sufficient quantity), the LED can also work as a data transceiver. Placing the photodiode outside the IC die saves expensive on-chip area. With the photovoltaic cell placed out of the die, the die can be covered in optically opaque material because the powering light can induce latch-up and noise and increase leakage currents. Photon absorption is more efficient in direct bandgap materials of LEDs [e.g., aluminium gallium arsenide (AlGaAs)] in contrast to indirect bandgap materials (e.g., silicon) [137]. Record-level efficiency improvements in GaAs solar cells have been achieved in this way, stressing commonalities between efficient photovoltaic cell and LED designs [138]. An LED is also an efficient photovoltaic cell for a limited range of its wavelengths, which are about 20–30-nm shorter than the peak emission wavelength.

With the added benefits of LEDs, an improvement in a wireless and batteryless optoelectronic microsystem has been made by using it for both wireless powering and data transmission, as depicted in Figure 50. The use of a single LED having a die size of 350×350 μm^2 with the help of an IC (230×210 μm^2) and a storage capacitor (0.5×1 mm^2) resulted in a 1-mm^3 wireless and batteryless microsystem [139].

For transcutaneous implants, optical powering can be accomplished using light with wavelengths between 600 and 900 nm (called the *near-infrared window*), where hemoglobin absorbs weakly and penetration of light can reach a maximum depth of around 5 cm [140]. Experimental results show that the laser power level of 1 W/cm^2 drops to 1 mW/cm^2 (30-dB power loss) through 3.4-cm-thick bovine tissue when a 808-nm wavelength is used [141].

Design of Batteryless CMOS Sensors for RF-Powered WSNs

The WSN is a group of spatially dispersed sensors (nodes) to collect physical or environmental information and cooperatively pass that information through the network to a central location. A WSN has several applications, e.g., building monitoring and automation, health-care monitoring, air pollution monitoring, forest-fire detection, and water-quality monitoring. Normally, each network node comprises a radio transceiver, a microcontroller, sensors, and an energy source, usually a battery. The lifetime of most sensors is mainly limited by the autonomy of their batteries. There are several solutions for extending the life of batteries, among which we can include the harvesting of electromagnetic energy available in the environment. As semiconductor technologies
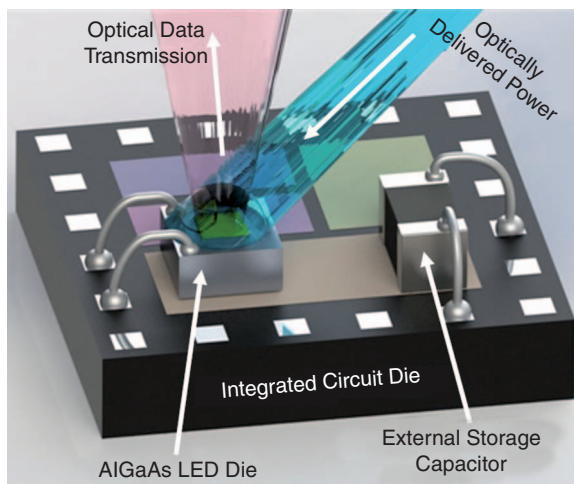

Figure 50. *A conceptual representation of an optically powered and optically transmitting microsystem using a single LED.*

evolve over time, not only the size of MOS transistors decreases toward nanometric scales; the circuits' power consumption is also considerably reduced. This trend favors the integration of several complex functions in a system-on-chip. It is thus possible to integrate complete ultralow-power autonomous sensors for RF-powered WSNs.

UMONS Microelectronics Laboratory is engaged in designing a wireless RF-powered temperature sensor. The architecture of the temperature sensor is depicted in Figure 51. RF energy is harvested with an receive antenna that is adapted to a rectifier/multiplier through an inductor/capacitor (LC) matching network to maximize energy transfer. The rectifier output charges an external capacitor that supplies the rest of the circuits on the chip. A power-management unit checks and regulates the minimum voltage level required across the external capacitor. It also controls the sensor working cycle by properly enabling/disabling each block in view of minimal power consumption. The temperature
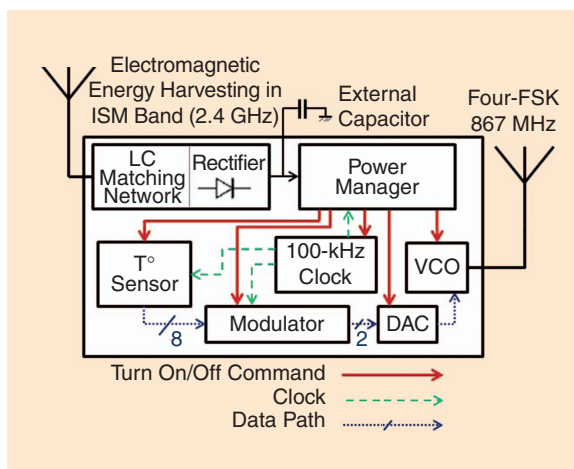

Figure 51. *A wireless and batteryless temperature sensor architecture.*

is measured with an ultralow-power temperature sensor that delivers a digital word to a modulator, which yields the transmission frame. The modulator output controls a voltage-controlled oscillator (VCO) through a digital-to-analog converter (DAC) to generate the four-FSK signal, which is transmitted by a transmit antenna. A 100-kHz master-clock generator provides the time reference for all digital circuits of the sensor. For a 15.6-ms long transmission frame at 50 kb/s, the bit error rate results in 10^{-4}. The system can operate at 0.5 V, while consuming 84 μW in on mode and 28.6 nW in idle mode. The achieved input sensitivity is −26 dBm.

The use of low-threshold voltage transistors available in the 65-nm CMOS technology allows a system capable of operating at ultralow voltage. This fact, together with the adopted design methodology [142], permitted significant reduction in power consumption and increase in rectifier sensitivity compared to prior works [143].

Acknowledgments

References

[1] M. Pinuela, D. C. Yates, S. Lucyszyn, and P. D. Mitcheson, "Maximizing DC-to-load efficiency for inductive power transfer," *IEEE Trans. Power Electron.*, vol. 28, no. 5, pp. 2437–2447, May 2013.

[2] M. S. Trotter, J. D. Griffin, and G. D. Durgin, "Power-optimized waveforms for improving the range and reliability of RFID systems," in *Proc IEEE Int. Conf. RFID*, 27–28 Apr. 2009, pp. 80–87.

[3] A. S. Boaventura and N. B. Carvalho, "Maximizing dc power in energy harvesting circuits using multisine excitation," in *Proc. IEEE MTT-S Int. Microwave Symp. Digest*, Jun. 5–10, 2011.

[4] A. Collado and A. Georgiadis, "Improving wireless power transmission efficiency using chaotic waveforms," in *Proc. IEEE MTT-S Int. Microwave Symp. Digest*, Montreal, 17–22 June 2012.

[5] A. Collado and A. Georgiadis, "Optimal waveforms for efficient wireless power transmission," *IEEE Microwave Wireless Compon Lett.*, vol. 24, no. 5, pp. 354–356, May 2014.

[6] A. Georgiadis, A. Collado, and K. Niotaki, "Rectenna design and signal optimization for electromagnetic energy harvesting and wireless power transfer,"' *IEICE Trans. Electron.*, vol. E98-C, no. 07, pp. 608–612, July 2015.

[7] H. Sakaki, S. Yoshida, K. Nishikawa, and S. Kawasaki, "Analysis of rectifier operation with FSK modulated input signal," in *Proc. IEEE Wireless Power Transfer Conf.*, May 2013, pp. 187–190.

[8] G. Fukuda, S. Yoshida, Y. Kai, N. Hasegawa, and S. Kawasaki, "Evaluation on use of modulated signal for microwave power transmission," in *Proc. 44th European Microwave Conf.*, Oct. 2014, pp. 425–428.

[9] J. Blanco, F. Bolos, A. Collado, and A. Georgiadis, "RF-energy harvesting and wireless power transfer efficiency from digitally modulated signals," in *Proc. IEEE 15th Mediterranean Microwave Symp.*, Lecce, Italy, 2015.

[10] A. Boaventura, D. Belo, R. Fernandes, A. Collado, A. Georgiadis, and N. B. Carvalho, "Boosting the efficiency: Unconventional waveform design for efficient wireless power transfer," *IEEE Microwave Mag.*, vol. 16, no. 3, pp. 87–96, Apr. 2015.

[11] C. H. P. Lorenz, S. Hemour, W. Liu, A. Badel, F. Formosa, and K. Wu, "Hybrid power harvesting for increased power conversion efficiency," *IEEE Microwave Wireless Compon. Lett.*, vol. 25, no. 10, pp. 687–689, Oct. 2015.

[12] M. Virili, A. Georgiadis, A. Collado, K. Niotaki, P. Mezzanotte, L. Roselli, F. Alimenti, and N. B. Carvalho, "Performance improvement of rectifiers for WPT exploiting thermal energy harvesting," *Wireless Power Transfer*, vol. 2, no. 1, pp. 22–31, Mar. 2015.

[13] D. Belo and N. Borges Carvalho, "Harmonic spaced multisines for efficient wireless power transmission," in *Proc. IEEE Wireless Power Transfer Conf.*, Boulder, May 2015

[14] D. Belo, J.-M. Munoz-Ferreras, R. Gomez-Garcia, and N. Borges Carvalho, "Exploiting radar waveforms for wireless power transmission," in *Proc. IEEE Wireles Power Transfer Conf.*, Boulder, May 2015.

[15] A. Boaventura, N. B. Carvalho, and A. Georgiadis, "The impact of multisine tone separation on RF-DC efficiency," in *Proc. Asia-Pacific Microwave Conf.*, 4–7 Nov. 2014, pp. 606–609.

[16] N. Pan, A. Boaventura, M. Rajabi, D. Schreurs, N. B. Carvalho, and S. Pollin, "Amplitude and frequency analysis of multisine wireless power transfer," in *Proc. Int. Workshop Integrated Nonlinear Microwave and Millimetere-wave Circuits Conf.*, Oct. 2015.

[17] Federal Communications Commission. "Revision of part 15 of the Commission's Rules Regarding Ultra-Wideband Transmission Systems, First Rep. Order (ET Docket 98-153)," Adopted Feb. 14, 2002. Released Apr. 22, 2002.

[18] Electronic Communications Committee (ECC). "Specific UWB Applications in the bands 3.4-4.8 GHz and 6.8-8.5 GHz Location Tracking Applications for Emergency Services (LAES), Location Tracking Applications Type 2 (LT2) and Location Tracking and Sensor Applications for Automotive and Transportation Environments (LTA), Oct. 2011.

[19] S. Lemey and H. Rogier, "SIW textile antennas as a novel technology for UWB RFID tags," in *Proc. IEEE RFID Technology and Applications Conf.*, Sept. 2014, pp. 256–260.

[20] O. Caytan, S. Lemey, S. Agneessens, D. Vande Ginste, P. Demeester, C. Loss, R. Salvado, and H. Rogier, "Half-mode substrate-integrated-waveguide cavity-backed slot antenna on cork substrate," *IEEE Antenn. Wireless Propagat. Lett.*, 2015. doi: 10.1109/LAWP.2015.2435891.

[21] R. Moro, S. Agneessens, H. Rogier, A. Dierck, and M. Bozzi, "Textile microwave components in substrate integrated waveguide technology," *IEEE Trans. Microwave Theory Tech.*, vol. 63, no. 2, pp. 422–432, Feb. 2015.

[22] S. Lemey, F. Declercq, and H. Rogier, "Textile antennas as hybrid energy harvesting platforms," *Proc. IEEE*, vol. 102, no. 11, pp. 1833–1857, Nov. 2014.

[23] T. Cuyckens and H. Rogier, "Framework for the simulation of wireless power transmission over ultra wide band links in multipath propagation environments in the vicinity of the human body," *Int. J. Numer. Model. Electron. Netw. Devices Field*, vol. 28, Mar. 2015. doi: 10.1002/jnm.2070.

[24] G. Stockman, H. Rogier, and D. Vande Ginste, "Dedicated model for the efficient assessment of wireless power transfer in the radiative near-field," *Int. J. Numer. Model. Electron. Netw. Devices Field*, vol. 28, Apr. 2015. doi: 10.1002/jnm.2075.

[25] [Online] Available: www.ti.com/lit/ds/symlink/bq25570.pdf

[26] H.J. Visser and S. Keyrouz, "Radiative RF Power Transfer Solutions for Wireless Sensors," in *Proc. IEEE Int. Symp. Antennas and Propagation*, Memphis, TN, 2014, pp. 1401–1402.

[27] [Online] Available: http://arduino.cc/en/main/arduinoboard-mega2560

[28] H. J. Visser, H. W. Pflug, and S. Keyrouz, "Rectenna demonstrators at Holst Centre/imec and Eindhoven University of Technology,"

in *Proc. European Conf. Antennas and Propagation*, Lisbon, Portugal, 2015, pp. 44.

[29] M. Stoopman, S. Keyrouz, H.J. Visser, K. Philips and W.A. Serdijn, "A self-calibrating RF energy harvester generating 1V at –26.3-DBm," in *Proc. Symp. VLSI Circuits*, 2013, pp. C226–C227.

[30] A. Takacs, H. Aubert, S. Fredon, L. Despoisse, and H. Blondeaux, "Microwave power harvesting for satellite health monitoring," *IEEE Trans. Microwave Theory Tech.*, vol. 62, no. 4, pp. 1090–1098, Apr. 2014.

[31] [Online] Available: www.laas.fr

[32] Z. Popovic, E. A. Falkenstein, D. Costinett, and R. Zane, "Low-power far-field wireless powering for wireless sensors," in *Proc. IEEE*, vol. 101, no. 6, pp. 1397–1407, June 2013.

[33] A. Takacs, H. Aubert, and S. Charlot, "Ultra-compact Ku band rectenna," in *Proc. IEEE MTT-S Int. Microwave Symp.*, Phoenix, June, 2015, pp. 17–22.

[34] A. Massa, G. Oliveri, F. Viani, and P. Rocca, "Array designs for long-distance wireless power transmission—State-of-the-art and innovative solutions," *IEEE Proc.*, vol. 101, no. 6, pp. 1464–1481, June 2013.

[34a] P. Rocca, G. Oliveri, R. J. Mailloux, and A. Massa, "Unconventional phased array architectures and design methodologies: A review," in *Proc. IEEE*, vol. 104, no. 3, pp. 544–560, Mar. 2016.

[35] P. E. Glaser, "The potential of satellite solar power," in *Proc. IEEE*, vol. 65, no. 8, pp. 1162–1176, Aug. 1977.

[36] G. Oliveri, L. Poli, and A. Massa, "Maximum efficiency beam synthesis of radiating planar arrays for wireless power transmission," *IEEE Trans. Antenn. Propagat.*, vol. 61, no. 5, pp. 2490–2499, May 2013.

[37] G. Franceschetti, P. Rocca, F. Robol, and A. Massa, "Innovative rectenna design for space solar power systems," in *Proc. IEEE MTT-S Int. Microwave Workshop Series on "Innovative Wireless Power Transmission: Technologies, Systems, and Applications,"* Kyoto, Japan, May 2012, pp. 151–153.

[38] P. Rocca, G. Oliveri, and A. Massa, "Array synthesis for optimal wireless power systems," in *Proc. IEEE AP-S Int. Symp. and USNC-URSI Radio Science Meeting*, Memphis, Tennessee, July 2014, pp. 1407–1408 (Invited paper).

[39] L. Manica, P. Rocca, and A. Massa, "Design of subarrayed linear and planar array antennas with SLL control based on an excitation matching approach," *IEEE Trans. Antenn. Propagat.*, vol. 57, no. 6, pp. 1684–1691, Jun. 2009.

[40] F. Viani, G. Oliveri, and A. Massa, "Compressive sensing pattern matching techniques for synthesizing planar sparse arrays," *IEEE Trans. Antennas Propagat.*, vol. 61, no. 9, pp. 4577–4587, Sept. 2013.

[41] A. G. Dimitriou, A. Bletsas, and J. N. Sahalos, "Room coverage improvements of UHF RFID with commodity hardware," *IEEE Trans. Antennas Propagat.*, vol. 53, no. 1, pp. 175–194, Feb. 2011.

[42] A. G. Dimitriou, A. Bletsas, A. Polycarpou, and J. N. Sahalos, "Theoretical findings and measurements on planning a UHF RFID system inside a room," *Radioeng. J.*, vol. 20, no. 2, pp. 387–397, June 2011.

[43] I. T. Markakis, T. Samaras, A. C. Polycarpou, and J. N. Sahalos, "An RFID-enabled Library Management System using Low-SAR Smart Bookshelves," in *Proc. Int. Conf. Electromagnetics Advanced Applications*, Torino, Italy, Sept. 2013, pp. 227–230.

[44] A. G. Dimitriou, S. Siachalou, A. Bletsas, and J. N. Sahalos, "A site-specific stochastic propagation model for passive UHF RFID," *IEEE Antenn. Wireless Propagat. Lett.*, vol. 13, pp. 623–626, Mar. 2014.

[45] A. G. Dimitriou, S. Siachalou, A. Bletsas, and J. N. Sahalos, "Site-specific stochastic propagation model for automated RFID network planning," in *Proc. Int. Conf. Electromagnetics Advanced Applications*, Torino, Italy, Sept. 2013, pp. 603–606.

[46] A. G. Dimitriou, A. Boursianis, I. Markakis, S. Siachalou, T. Samaras, and J. N. Sahalos, "Comparison of a fast probabilistic propagation model against an analytical computational-EM model and measurements for the evaluation of passive RFID systems," in

Proc. 9th European Conf. Antennas and Propagation, Lisbon, Portugal, Apr. 2015.

[47] A. G. Dimitriou, S. Siachalou, A. Bletsas, and J. N. Sahalos, "Automated RFID network planning with site-specific stochastic modeling and particle swarm optimization," in *Proc. IEEE RFID Technology and Applications Conf.*, Tampere, Finland, Sept. 2014, pp. 44–49.

[48] M. Dionigi and M. Mongiardo, "Numerical electromagnetic modelling of a wireless power transfer system," in *Proc. IEEE Int. Conf. Numerical Electromagnetic Modeling and Optimization for RF, Microwave, and Terahertz Applications*, May 2014, pp. 1–8.

[49] M. Dionigi, M. Mongiardo, and R. Perfetti, "Rigorous network and fullwave electromagnetic modeling of wireless power transfer links," *IEEE Trans. Microwave Theory Tech.*, vol. 63, no. 1, pp. 65–75, Jan. 2015.

[50] A. Kurs, A. Karalis, R. Moffatt, J. D. Joannopoulos, P. Fisher, and M. Soljacic, "Wireless power transfer via strongly coupled magnetic resonances," *Science*, vol. 317, no. 5834, pp. 83–86, 2007.

[51] A. Costanzo, M. Dionigi, M. Masotti, M. Mongiardo, G. Monti, L. Tarricone, and R. Sorrentino, "Electromagnetic energy harvesting and wireless power transmission: A unified approach," in *Proc. IEEE*, vol. 102, no. 11, pp. 1692–1711, Nov. 2014.

[52] A. Costanzo, M. Dionigi, F. Mastri, M. Mongiardo, J. A. Russer, and P. Russer, "Rigorous design of magnetic-resonant wireless power transfer links realized with two coils, in *Proc. European Microwave Conf.*, Rome, Italy, 2014, pp. 414–417.

[53] A. Costanzo, M. Dionigi, F. Mastri, M. Mongiardo, J. A. Russer, and P. Russer, "Rigorous network modeling of magnetic-resonant wireless power transfer," *Wireless Power Transfer*, vol. 1, no. 1, pp. 27–34, 2014.

[54] J. Russer and P. Russer, "Design considerations for a moving field inductive power transfer system," in *Proc. IEEE Wireless Power Transfer*, May 2013, pp. 147–150.

[55] J. A. Russer, M. Dionigi, M. Mongiardo, and P. Russer, "A moving field inductive power transfer system for electric vehicles," in *Proc. IEEE European Microwave Conf.*, Nuremberg, Germany, Oct. 2013, pp. 519–522.

[56] J. A. Russer, M. Dionigi, M. Mongiardo, and P. Russer, "A bidirectional moving field inductive power transfer system for electric vehicles," in *Proc. 11th IEEE Int. Conf. Telecommunication in Modern Satellite, Cable and Broadcasting Services*, Oct. 2013, vol. 1, pp. 17–20.

[57] J.A. Russer M. Dionigi, M. Mongiardo, F. Mastri, A. Costanzo, and P. Russer, "A system for dynamic inductive power supply of electric vehicles on the road," in *Proc. IEEE Wireless Power Transfer Conf.*, Aveiro, 2016.

[58] G. Monti, L. Tarricone, and C. Trane, "Experimental characterization of a 434 mhz wireless energy link for medical applications," *Prog. Electromagnet. Res. C*, vol. 30, pp. 53–64, May 2012.

[59] G. Monti, P. Arcuti, and L. Tarricone, "Resonant inductive link for remote powering of pacemakers," *IEEE Trans. Microwave Theory Tech.*, vol. 63, no. 11, pp. 3814–3822.

[60] G. Monti, M. D. Paolis, and L. Tarricone, "Wireless energy link for deep brain stimulation," in *Proc. European Microwave Conf.*, Paris, France, Sept. 2015, pp. 1–4.

[61] G. Monti, M. D. Paolis, and L. Tarricone, "Wireless power transfer link for rechargeable deep brain stimulators," in *Proc. Mediterranean Microwave Symp.*, Lecce, Italy, 2015, pp. 1–4.

[62] F. Mastri, A. Costanzo, M. Dionigi, and M. Mongiardo, "Harmonic balance design of wireless resonant-type power transfer links," in *Proc. IEEE MTT-S Int. Microwave Workshop Series on Innovative Wireless Power Transmission: Technologies, Systems, and Applications*, 2012, pp. 245–248.

[63] A. Costanzo, M. Dionigi, F. Mastri, and M. Mongiardo, "Rigorous modeling of mid-range wireless power transfer systems based on Royer oscillators," in *Proc. IEEE Wireless Power Transfer*, pp. 69–72, 2013.

[64] [Online] Available: http://www.qinside.biz/en/support/qi-enabled-phones-2015

[65] [Online] Available: http://www.wirelesspowerconsortium.com

[66] [Online] Available: http://a4wppmamerge.com/Release.pdf

[67] B. Thoen and N. Stevens, "Development of a communication scheme for wireless power applications with moving receivers," *IEEE Trans. Microwave Theory Tech.*, vol. 63, no. 3, pp. 857–863, Mar. 2015.

[68] [Online] Technical specifications. Available: http://www.logitech.com/en-us/product/marathon-mouse-m705

[69] S. Wielandt, B. Thoen, J. Goemaere, D. Strycker, and N. Stevens, "Inductive charging of an EDLC powered wristband device for medical measurements," in *Proc. 22nd IEEE European Conf. Circuit Theory and Design,* Trondheim, Norway, Aug. 2015.

[70] [Online] Available: http://www.bellaag.com

[71] K. Finkenzeller, *RFID Handbook: Fundamentals and Applications in Contactless Smart Cards and Identification*, 2nd ed. New York: Wiley, 2005.

[71a] J. Kracek, M. Svanda, M. Mazanek, and J. Machac, "Implantable semi-active UHF RFID tag with inductive wireless power transfer," *IEEE Antenn. Wireless Propagat. Lett.*, vol. 15, pp. 1657–1660, 2016.

[72] J. Kracek and M. Mazanek, "Wireless power transmission for power supply: State of art," *Radioengineering*, vol. 20, no. 2, pp. 457–463, 2011.

[73] R. B. Wynn, et al. "Autonomous Underwater Vehicles (AUVs): Their past, present and future contributions to the advancement of marine geoscience," *Mar. Geol.*, vol. 352, pp. 451–468, 2014.

[74] N. A. Cruz and A. C. Matos, "The MARES AUV, a modular autonomous robot for environment sampling," in *Proc. IEEE Oceanic Engineering Society*, Sept. 2008, pp. 1–6.

[75] T. Kojiya, F. Sato, H. Matsuki, et al. "Automatic power supply system to underwater vehicles utilizing non- contacting technology," in *Proc. IEEE Oceanic Engineering Society*, 2004, pp. 2341–2345.

[76] M. Kesler and C. McCarthy, "Highly resonant wireless power transfer in subsea applications," Witricity white paper, 2013.

[77] Z.-S. Li, D-J. Li, L. Lin, and Y. Chen, "Design considerations for electromagnetic couplers in contactless power transmission systems for deep-sea applications," *J. Zhejiang Univ. Sci. C*, vol. 11, no. 10, pp. 824–834, 2010.

[78] J.-G. Shi, D-J. Li, and C.-J. Yang, "Design and analysis of an underwater inductive coupling power transfer system for autonomous underwater vehicle docking applications," *J. Zhejiang Univ. Sci. C*, vol. 15, no. 1, pp. 51–62, 2014.

[79] K. Shizuno, S. Yoshida, M. Tanomura, and Y. Hama, "Long distance high efficient underwater wireless charging system using dielectric-assist antenna," in *Proc. IEEE Oceanic Engineering Society*, 2014, pp. 1–3.

[80] R. D. Fernandes, J. N. Matos, and N. B. Carvalho, "Behavior of resonant electrical coupling in terms of range and relative orientation," in *Proc. IEEE Wireless Power Transfer Conf.*, 2014, pp. 118–121.

[81] R. D. Fernandes, J. N. Matos, and N. B. Carvalho, "Resonant electrical coupling: circuit model and first experimental results," *IEEE Trans. Microwave Theory Tech.*, vol. 63, no. 9, pp. 2983–2990, Sept. 2015.

[82] R. D. Fernandes, J. N. Matos, and N. B. Carvalho, "Constructive combination of resonant magnetic coupling and resonant electrical coupling," in *Proc. IEEE Wireless Power Transfer Conf.*, Boulder, CO, May, 2015.

[83] C. Yang and K. Tsunekawa, "Analysis and performance improvement of independent electric coupled resonance WPT system with impedance transformer," in *Proc. IEEE Wireless Power Transfer Conf.*, 2014, pp. 239–242.

[84] R. B. Wynn, et al. "Autonomous underwater vehicles (AUVs): Their past, present and future contributions to the advancement of marine geoscience," *Mar. Geol.*, vol. 352, pp. 451–468, 2014.

[85] L. Roselli, N. Borges Carvalho, F. Alimenti, P. Mezzanotte, G. Orecchini, M. Virili, C. Mariotti, R. Goncalves, and P. Pinho, "Smart surfaces: Large area electronics systems for internet of things enabled by energy harvesting," in *Proc. IEEE*, vol. 102, no. 11, pp. 1723–1746, Nov. 2014.

[86] B. Cook, C. Mariotti, J. Cooper, D. Revier, B. Tehrani, L. Aluigi, L. Roselli, and M. Tentzeris, "Inkjet-printed, vertically-integrated, high performance inductors and transformers on flexible LCP substrate," in *Proc. IEEE MTT-S Int. Microwave Symp.*, 2014.

[87] F. Alimenti, P. Mezzanotte, M. Dionigi, M. Virili, and L. Roselli, "Microwave circuits in paper substrates exploiting conductive adhesive tapes," *IEEE Microwave Wireless Compon. Lett.*, vol. 22, no. 12, pp. 660–662, Dec. 2012.

[88] C. Mariotti, R. Gonalves, L. Roselli, N. Carvalho, and P. Pinho, "Energy evaporation": The new concept of indoor systems for wpt and eh embedded into the floor," in *Proc. IEEE Int. Microwave Symp.*, 2015.

[89] S. Nikoletseas and T. P. Raptis, "Efficient protocols for wireless power transfers in ad hoc networks," in *Cyber-Physical Systems*. Boca Raton, FL: CRC, 2015, pp. 527–558.

[90] S. Nikoletseas and T. P. Raptis, "Efficient algorithms for characteristic wireless power transfer problems in sensor networks," in *Lecture Notes of the Institute for Computer Sciences, Social Informatics and Telecommunications Engineering*. New York: Springer-Verlag, 2014, vol. 140, pp. 204–215.

[91] C. M. Angelopoulos, S. Nikoletseas, T. P. Raptis, C. Raptopoulos, and F. Vasilakis. "Efficient energy management in wireless rechargeable sensor networks," in *Proc. 15th ACM Int. Conf. Modeling, Analysis and Simulation of Wireless and Mobile Systems*, 2012. pp. 309–316.

[92] C. M. Angelopoulos, S. Nikoletseas, and T. P. Raptis, "Wireless energy transfer in sensor networks with adaptive, limited knowledge protocols," *Comput. Netw.*, vol. 70, pp. 113–141, Sept.2014.

[93] A. Madhja, S. Nikoletseas, and T. P. Raptis, "Distributed wireless power transfer in sensor networks with multiple mobile chargers," *Comput. Netw.*, vol. 80, pp. 89–108, Apr. 2015.

[93a] C. Wang, J. Li, F. Ye, and Y. Yang, "Multi-vehicle coordination for wireless energy replenishment in sensor networks," in *Proc. 27th IEEE Int. Parallel & Distributed Processing Symp.*, 2013, pp. 1101–1111.

[94] A. Madhja, S. Nikoletseas, and T. P. Raptis, "Hierarchical, collaborative wireless energy transfer in sensor networks with multiple mobile chargers," *Comput. Netw.*, vol. 97, pp. 98–112, Mar. 2016.

[95] S. Nikoletseas, T. P. Raptis, and C. Raptopoulos, "Low radiation efficient wireless energy transfer in wireless distributed systems," in *Proc. 34th IEEE Int. Conf. Distributed Computing Syst.*, 2015, pp. 196–204.

[96] S. Nikoletseas, T. P. Raptis, A. Souroulagkas, and D. Tsolovos, "An experimental evaluation of wireless power transfer protocols in mobile ad hoc networks," in *Proc. IEEE Wireless Power Transfer Conf.*, 2015, pp. 1–3.

[97] S. Riviere, "An integrated model of a wireless power transportation for RFID and WSN applications," in *Proc. 16th IEEE Int. Conf. Electronics, Circuits, and Systems*, Dec. 2009, pp. 235–238.

[98] S. Riviere, "Study of complete WPT system for WSN applications at low power level," *Electron. Lett.*, vol. 46, no. 8, pp. 597–598, 2010.

[99] M. Roberg, T. Reveyrand, I. Ramos, E. Falkenstein, and Z. Popovic, "High-efficiency harmonically terminated diode and transistor rectifiers," *IEEE Trans. Microwave Theory Tech.*, vol. 60, no. 12, pp. 4043–4052, 2012.

[100] R. Scheeler, S. Korhummel, and Z. Popovic, "A dual-frequency ultralow-power efficient 0.5-g rectenna," *IEEE Microwave Mag.*, vol. 15, no. 1, pp. 109–114, Jan. 2014.

[101] A. Georgiadis, G. Andia, and A. Collado, "Rectenna design and optimization using reciprocity theory and harmonic balance analysis for electromagnetic (EM) energy harvesting," *IEEE Antenn. Wireless Propagat. Lett.*, vol. 9, pp. 444–446, 2010.

[102] G. Andia Vera, Y. Duroc, and S. Tedjini, "Analysis of harmonics in UHF RFID signals," *IEEE Trans. Microwave Theory Tech.*, vol. 61, no. 6, pp. 2481–2490, 2013.

[103] S. Ladan and K. Wu, "35 GHz harmonic harvesting rectifer for wireless power transmission," in *Proc. IEEE MTT-S Int. Microwave Symp. Digest*, June 2014, pp. 1–3.

[104] G. Andia Vera, Y. Duroc, and S. Tedjini, "RFID test platform: nonlinear characterization," *IEEE Trans. Instrum. Measure.*, vol. 63, no. 9, pp. 2299–2305, Sept. 2014.

[105] A. Boaventura and N. Carvalho, "Maximizing dc power in energy harvesting circuits using multisine excitation," in *Proc. IEEE MTT-S Int. Microwave Symp. Digest*, June 2011, pp. 1–4.

[106] M. Trotter, J. Griffin, and G. Durgin, "Power-optimized waveforms for improving the range and reliability of rfid systems," in *Proc. IEEE Int. Conf. RFID*, Apr. 2009, pp. 80–87.

[107] A. Collado and A. Georgiadis, "Optimal waveforms for efficient wireless power transmission," *IEEE Microwave Wireless Compon. Lett.*, vol. 24, no. 5, pp. 354–356, May 2014.

[108] NXP. Ucode g2xm and g2xl product data sheet company public. [Online]. Available: http://www.nxp.com/documents/data sheet/SL3ICS1002 1202.pdf

[109] Impinj Monza 5. Impinj uhf rfid product downloads – monza tag chips. [Online]. Available: http://www.impinj.com

[110] G. Andia-Vera, A. Georgiadis, Y. Duroc and S. Tedjini, "Cooperative integration of harvesting sections for passive RFID communication," in *Proc IEEE MTT-S Int. Microwave Symp.*, Phoenix, AZ, May 2015.

[111] A. C. Polycarpou, T. Samaras, and J. N. Sahalos, "An RFID-based library management system using smart cabinets: A pilot project," in *Proc. 8th European Conf. Antennas & Propagation*, 2014, pp. 2954–2955.

[112] A. C. R. Medeiros, J. R. Costa, and C. A. Fernandes, "RFID reader antennas for tag detection in self-confined volumes at UHF," *IEEE Antenn. Propagat. Mag.*, vol. 53, no. 2, pp. 39–50, Apr. 2011.

[113] A. Christ, W. Kainz, E. G. Hahn, K. Honegger, M. Zefferer, E. Neufeld, W. Rascher, R. Janka, W. Bautz, J. Chen, B. Kiefer, P. Schmitt, H. P. Hollenbach, J. Shen, M. Oberle, D. Szczerba, A. Kam, J. W. Guag, and N. Kuster, "The virtual family—Development of surface-based anatomical models of two adults and two children for dosimetric simulations," *Phys. Med. Biol.*, vol. 55, no. 2, pp. 23–38, 2010.

[114] S. Gabriel, R. W. Lau, and C. Gabriel, "The dielectric properties of biological tissues: III. Parametric models for the dielectric spectrum of tissues," *Phys. Med. Biol.*, vol. 41, no. 11, pp. 2271–2293, Nov. 1996.

[115] SEMCAD, Schmid & Partner Engineering AG (SPEAG) [Online]. Available: http://www.semcad.com

[116] A. Pantelopoulos and N. G. Bourbakis, "A survey on wearable sensor-based systems for health monitoring and prognosis," *IEEE Trans. Syst. Man. Cybern. Syst. Rev.*, vol. 40, no. 1, pp. 1–12, 2010.

[117] J. Walk, J. Weber, C. Soell, R. Weigel, G. Fischer, and T. Ussmueller, "Remote powered medical implants for telemonitoring," in *Proc. IEEE*, vol. 102, no. 11, pp. 1811–1832, 2014.

[118] K. D. Wise, D. J. Anderson, J. F. Hetke, D. R. Kipke, and K. Najafi, "Wireless implantable microsystems: high-density electronic interfaces to the nervous system.," in *Proc. IEEE*, vol. 92, no. 1, pp. 76–97, 2004.

[119] T. Schanze, L. Hesse, C. Lau, N. Greve, W. Haberer, S. Kammer, T. Doerge, A. Rentzos, and T. Stieglitz, "An optically powered single channel stimulation implant as test system for chronic biocompatibility and biostability of miniaturized retinal vision prostheses," *IEEE Trans. Biomed. Eng.*, vol. 54, no. 6, pp. 983–992, June 2007.

[120] S. Fandrey, S. Weiss, and J. Muller, "Development of an active intravascular MR device with an optical transmission system," *IEEE Trans. Med. Image*, vol. 27, no. 12, pp. 1723–1727, Dec. 2008.

[121] J. A. Potkay, "Long term, implantable blood pressure monitoring systems," *Biomed. Microdevices*, vol. 10, no. 3, pp. 379–392, 2008.

[122] M. Allen, M. Fonseca, J. White, J. Kroh, and D. Stern, "Implantable wireless sensor for blood pressure measurement with an artery 2005," CardioMEMS, Inc.

[123] A. D. DeHennis and K. D. Wise, "A wireless microsystem for the remote sensing of pressure, temperature, and relative humidity," *J. Microelectromech. Syst.*, vol. 14, no. 1, pp. 12–22, 2005.

[124] A. S. Y. Poon, O'Driscoll. Stephen, and T. H. Meng, "Optimal frequency for wireless power transmission into dispersive tissue," *IEEE Trans. Antenn. Propagat.*, vol. 58, no. 5, pp. 1739–1750, 2010.

[125] K. V. S. Rao, P. V. Nikitin, and S. F. Lam, "Antenna design for UHF RFID tags: A review and a practical application," *IEEE Trans. Antenn. Propagat.*, vol. 53, no. 12, pp. 3870–3876, Dec. 2005.

[126] P. Pursula, T. Vaha-Heikkila, A. Muller, D. Neculoiu, G. Konstantinidis, A. Oja, and J. Tuovinen, "Millimeter-wave identification—A new short-range radio system for low-power high data-rate applications," *IEEE Trans. Microwave Theory Tech.*, vol. 56, no. 10, pp. 2221–2228, Oct. 2008.

[127] B. W. Cook, S. Lanzisera, and K. S. J. Pister, "SoC issues for RF smart dust," in *Proc. IEEE*, vol. 94, no. 6, pp. 1177–1196, June 2006.

[128] S. O'Driscoll, P. Ada, and T. H. Meng, "A mm-sized implantable power receiver with adaptive link compensation," in *Proc. IEEE Int. Solid-State Circuits Conf. Digest Technical Papers*, 2009.

[129] I. Lee, Y. Kim, S. Bang, G. Kim, H. Ha, Y.-P. Chen, D. Jeon, et al. "Circuit techniques for miniaturized biomedical sensors," in *Proc. IEEE Custom Integrated Circuits Conf.*, 2014, pp. 1–7.

[130] K. E. Laflin, C. J. Morris, N. Bassik, M. Jamal, and D. H. Gracias, "Tetherless microgrippers with transponder tags," *J. Microelectromech. Syst.*, vol. 20, no. 2, pp. 505–511, Apr. 2011.

[131] E. J. Robinson, F. D. Smith, K. M. Sullivan, and N. R. Franks, "Do ants make direct comparisons?," in *Proc. Biol. Sci.*, vol. 276, no. 1667, pp. 2635–2641, July 2009.

[132] M. H. Ghaed, G. Chen, R-U. Haque, M. Wieckowski, Y. Kim, G. Kim, Y. Lee, et al. "Circuits for a cubic-millimeter energy-autonomous wireless intraocular pressure monitor," *IEEE Trans. Circuits Syst. I, Reg. Papers.*, vol. 60, no. 12, pp. 3152–3162, 2013.

[133] G. Kim, L. Yoonmyung, F. Zhiyoong, P. Pat, K. Ye-Sheng, K. Ben, G. Mohammad Hassan, et al. "A millimeter-scale wireless imaging system with continuous motion detection and energy harvesting," in *Proc. Symp. VLSI Circuits Digest of Technical Papers*, 2014, pp. 1–2.

[134] O. Aktan, B. Sarioglu, U. Cindemir, S. Onur Unlu, G. Dundar, S. Mutlu, and A. D. Yalcinkaya, "Optoelectronic CMOS power supply unit for electrically isolated microscale applications," *IEEE J. Sel. Top. Quantum Electron.*, vol. 17, no. 3, pp. 747–756, May/June 2011.

[135] B. Sarioglu, O. Aktan, A. Oncu, S. Mutlu, G. Dundar, and A. D. Yalcinkaya, "An optically powered CMOS receiver system for intravascular magnetic resonance applications," *IEEE Trans. Emerg. Sel. Topics Circuits Syst.*, vol. 2, no. 4, pp. 683–691, 2012.

[136] B. A. Warneke, M. D. Scott, B. S. Leibowitz, L. Zhou, C. L. Bellew, J. A. Chediak, J. M. Kahn, B. E. Boser, and K. S. J. Pister, "An autonomous 16 mm3 solar-powered node for distributed wireless sensor networks," in *Proc. IEEE Sens.* vol. 2, pp. 1510–1515, 2002.

[137] P. Bhattacharya, *Semiconductor Optoelectronic Devices*. New Jersey: Prentice Hall, 1994.

[138] O. D. Miller, E. Yablonovitch, and S. R. Kurtz, "Strong internal and external luminescence as solar cells approach the Shockley–Queisser limit," *IEEE J. Photovolt.*, vol. 2, no. 3, pp. 303–311, July 2012.

[139] I. Haydaroglu and S. Mutlu, "Optical power delivery and data transmission in a wireless and batteryless microsystem using a single light emitting diode," *J. Microelectromech. Syst.*, vol. 24, no. 1, pp. 155–165, 2015.

[140] T. Vo-Dinh, Ed. *Biomedical Photonics Handbook: Biomedical Diagnostics*, vol. 2. Boca Raton, FL: CRC, 2014.

[141] D. E. Hudson, et al. "Penetration of laser light at 808 and 980 nm in bovine tissue samples," *Photomed. Laser Surg.*, vol. 31, no. 4, pp. 163–168, 2013.

[142] R. Fiorelli, "An all-inversion-region gm/ID based design methodology for radio frequency blocks in CMOS nanometer technologies," PhD dissertation, CNM Sevilla, Spain, Oct. 2011.

[143] G. Papotto, et al. "A 90-nm CMOS 5-Mbps crystal-less RF-powered transceiver for wireless sensor network nodes," *J. Solid-State Circuits*, vol. 49, no. 2, pp. 335–346, Feb. 2014.